SAND2018-2432J

A Silicon Metal-Oxide-Semiconductor Electron Spin-Orbit Qubit

Ryan M. Jock,[1,*] N. Tobias Jacobson,[2] Patrick Harvey-Collard,[1,3] Andrew M. Mounce,[1] Vanita Srinivasa,[2] Dan R. Ward,[1] John Anderson,[1] Ron Manginell,[1] Joel R. Wendt,[1] Martin Rudolph,[1] Tammy Pluym,[1] John King Gamble,[2] Andrew D. Baczewski,[2] Wayne M. Witzel,[2] and Malcolm S. Carroll[1,†]

[1] *Sandia National Laboratories, Albuquerque, NM 87185, USA*
[2] *Center for Computing Research, Sandia National Laboratories, Albuquerque, NM 87185, USA*
[3] *Département de physique et Institut quantique, Université de Sherbrooke, 2500 boul. de l'Université, Sherbrooke, QC, J1K 2R1, Canada*

The silicon metal-oxide-semiconductor (MOS) material system is a technologically important implementation of spin-based quantum information processing. However, the MOS interface is imperfect leading to concerns about $1/f$ trap noise and variability in the electron g-factor due to spin-orbit (SO) effects. Here we advantageously use interface-SO coupling for a critical control axis in a double quantum dot singlet-triplet qubit. The magnetic field orientation dependence of the g-factors is consistent with Rashba and Dresselhaus interface-SO contributions. The resulting all-electrical, two-axis control is also used to probe the MOS interface noise. The measured inhomogeneous dephasing time, $T_{2\mathrm{m}}^{\star}$, of 1.6 μs is consistent with 99.95% ^{28}Si enrichment. Furthermore, when tuned to be sensitive to exchange fluctuations, a quasi-static charge noise detuning variance of 2 μeV is observed, competitive with low-noise reports in other semiconductor qubits. This work, therefore, demonstrates that the MOS interface inherently provides properties for two-axis qubit control, while not increasing noise relative to other material choices.

* Corresponding author: rmjock@sandia.gov

† Corresponding author: mscarro@sandia.gov

INTRODUCTION

Spin qubits in silicon metal-oxide-semiconductor (MOS) structures offer a promising path towards implementing quantum information processing. The MOS system combined with enriched ^{28}Si provides a magnetic vacuum [1] and promises to leverage the extensive CMOS fabrication platform. Recently, several critical demonstrations have shown long spin coherence times [2], two-qubit couplings of single spins in a multi-quantum dot layout[3], large tunable valley-splitting[2, 4, 5] and importantly similar valley splittings in different process flows and multiple devices[4, 5]. Yet, there are persistent concerns about the intrinsically imperfect Si/SiO_2 interface produces persistent concerns about charge noise from the disordered interface. Two potentially key performance challenges identified are extra detrimental charge noise and variable g-factors[6, 7].

Charge traps and two-level fluctuators near the interface are believed to be potential sources of noise in MOS devices[8–10]. To attempt to suppress the challenges of disorder and trap noise Si QD spin qubits have also been developed in heteroepitaxial Si/SiGe[11–16]. The imperfect crystal-dielectric interface is shifted further away. This is the predominant choice despite reports of difficulties with small or variable valley splitting[13–15, 17]. Nevertheless qubits have successfully been demonstrated and charge noise has been studied in Si/SiGe qubits[12, 16, 18, 19], but only indirect measures of charge noise in MOS qubits have been reported[3, 20, 21]. Direct characterization of charge noise at the MOS interface is needed for comparison.

Variability in g-factors recently observed in silicon QDs is also feared to introduce potentially challenging complications for many-qubit device architectures[7]. In bulk Si, the spin-orbit (SO) interaction leads to only weakly perturbed electron g-factors that are close to $g = 2.0$. However, the inversion asymmetry of the crystal at an interface leads to a SO interaction[22–25], as shown in Fig. 1. When a magnetic field is applied with a component parallel to the interface, electron cyclotron motion establishes a non-zero net momentum component along the interface, Fig. 1(a). The coupling of the electron momentum perpendicular to the effective electric field at the interface produces the SO interaction. The vertical electric potential at the interface leads to a Rashba SO contribution due to structural inversion asymmetry (SIA). A second interaction, the Dresselhaus contribution, is attributed to microscopic interface inversion asymmetry (IIA)[26], due to the largely unknown and possibly position dependent inter-atomic electric fields at the Si/SiO_2 boundary. Recent work has attributed the variability in electron g-factor at silicon interfaces to spin-orbit coupling and interface disorder[2, 6, 27–30]. However, while the effects of vertical electric field and in-plane magnetic field direction have been observed, the full dependence on magnetic field strength and orientation has not, to date, been characterized in the MOS material system. We further note that this interface effect is not theoretically unique to Si MOS or SiGe/Si interfaces [22, 23, 31] and variability in g-factor has also been observed in GaAs/AlGaAs QDs[32, 33], as well as holes in silicon QDs[34]. Because of its strength and angular dependence, which is similar to bulk SO effects, it is possible that the contribution of the interface effect, particularly on the Dresselhaus coupling, is under-appreciated in other systems that leverage strong SO coupling. Improved understanding of this effect has the potential to influence areas such as spintronics and the pursuit of forming topological states of matter [35, 36].

In this work, we advantageously use the inherent g-factor difference from the SO coupling at the Si/SiO_2 interface to create a second axis of control for a double quantum dot (DQD) singlet-triplet (ST) qubit. This first demonstration of an all-electrical, two-axis controlled qubit in MOS is used to study qubit noise and SO interaction at the dielectric interface. One of the central results of this paper is a quantitative characterization of charge noise in a MOS qubit (e.g., quasi-static detuning variance and Hahn-echo time). The magnitudes are comparable if not better than those reported for other semiconductor qubit materials like GaAs/AlGaAs and Si/SiGe. The second central result of this paper is that we demonstrate a SO ST qubit and use its coherent qubit rotations to characterize the SO interaction at the MOS interface over its full magnetic field angular dependence. We observe that, by choice of external magnetic field orientation, the intrinsic SO interaction may be maximized to drive spin rotations or canceled out, which may be important for applications where uniform spin splitting between many QDs is necessary. In particular, an out-of-plane magnetic field orientation, measured in this work, should uniformly suppress the SO effect. We additionally extend the theoretical framework for the interface Rashba-Dresselhaus coupling providing a gauge independent phenomenological effective mass description of the full angular dependence that is in quantitative agreement with experiment. This work, therefore, further advances our understanding of the silicon MOS interface as a potential state-of-the-art platform for quantum information technologies.

RESULTS

Spin-orbit singlet-triplet qubit

The qubit in this work is formed within a MOS double quantum dot (DQD). Two electrons are electrostatically confined within a double well potential, where the dominant interaction between the electrons can be electrically

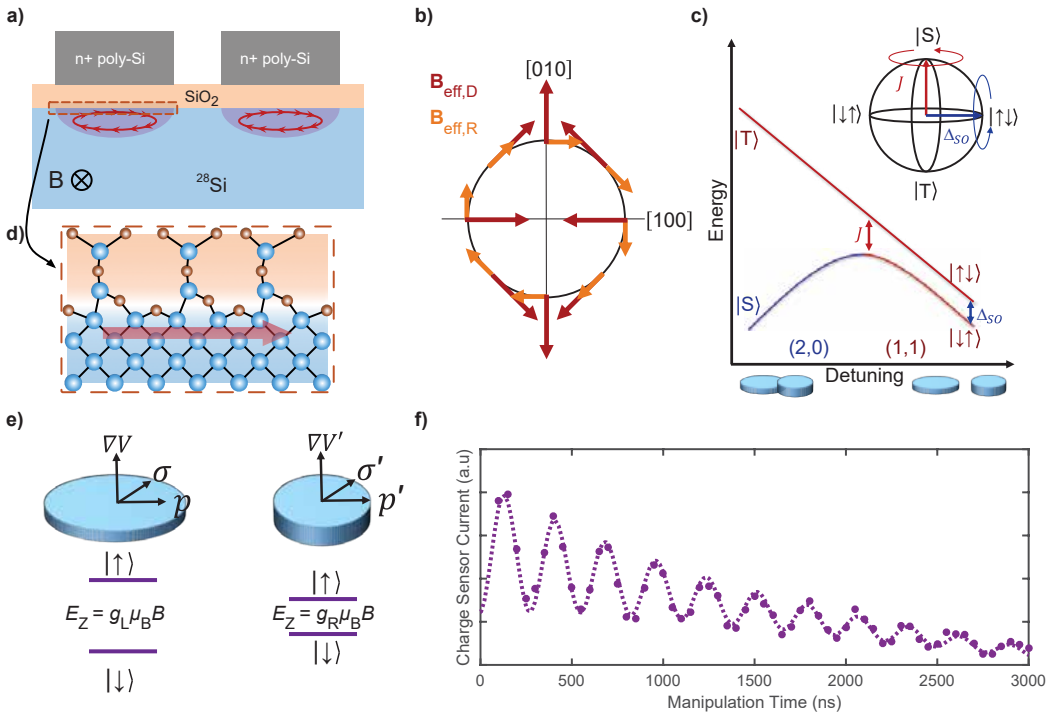

Fig. 1: **MOS spin-orbit driven singlet-triplet qubit**. a) Cartoon representation of the interface spin-orbit interaction. For an electron confined to a QD, an in-plane magnetic field will cause a finite momentum at the interface which, in the presence of broken inversion symmetry, leads to a spin-orbit interaction. The position of the QDs presented in this work, relative to the gates, differs from what is portrayed here (see Supplementary Fig. 2) b) Schematic example of the effective spin-orbit field due to the Dresselhaus (red) and Rashba (orange) interactions for in-plane electron momentum. c) Schematic energy diagram of the DQD near the (2,0) $\rightarrow$ (1,1) charge transition, showing the energy of the singlet and triplet states as a function of QD-QD detuning, ϵ. Near the interdot transition ($\epsilon = 0$), the exchange energy, J, dominates the electronic interaction and drives rotations about the Z-axis (red arrow in inset). Deep into the (1,1) charge sector ($\epsilon > 0$), J is small and the electronic states rotate about the X-axis due to a difference in Zeeman Energy between each QD (blue arrow in inset). d) Details of the interface at the inter-atomic bond level govern the spin-orbit interaction. e) The local electrostatic environment of each QD leads to different momenta and electric fields at the interface and, thus, distinct spin-orbit interactions and Zeeman energy splitting. f) Charge sensor current as a function of time spent deep in the (1,1) charge sector, where higher current indicates a higher probability of measuring a singlet state. The oscillations indicate clear X-rotations due to a difference in spin-orbit interaction in each QD.

tuned between two regimes for two-axis control, Fig. 1(c). When the electronic wave functions of the QDs overlap significantly, the exchange energy, J, dominates. When the two electrons are well separated, J is small and distinct Zeeman energies result from the differences in their interface SO coupling. The difference in SO coupling leads to a variation in effective electron g-factors, Fig. 1(e). This amounts to an effective magnetic field gradient between the QDs that can be tuned with control of the applied electric and magnetic fields. Thus, we achieve all-electrical two-axis control using native features of the MOS DQD system, avoiding the substantial fabrication complications to add a second axis of control for other Si qubit schemes.

We define the computational basis as the eigenstates of the two-spin system in the limit of a large singlet-triplet exchange energy, J. Specifically, these are the two states, S and T_0, of the $m = 0$ subspace, which form a decoherence-free subspace relative to fluctuations in a uniform magnetic field [37]. An applied magnetic field splits the $m = \pm 1$ spin triplet states ($T_{\pm}(1,1)$) and $m = 0$ states by the Zeeman energy $E_{\mathrm{Z}} = g\mu_{\mathrm{B}}B$ to isolate the $m = 0$ subspace. A qubit state can then be initialized in a singlet ground state when the two QDs are electrically detuned out of resonance such that it is preferable to have a $(N_{\mathrm{QD}_1}, N_{\mathrm{QD}_2}) = (2,0)$ charge state, Fig 1(c). Rapid adiabatic passage to the $(1,1)$ charge state produces a superposition of the S and T_0 eigenstates in the gradient field. A difference in the Larmor spin precession frequency of the two QDs induces X-rotations between the $S(1,1)$ and $T_0(1,1)$ states,

Fig. 1(f) and 2(a). For each QD the angular precession frequency is given by $\omega = g\mu_B B/\hbar$, where g is the electron g-factor, μ_B is the Bohr magneton, $\hbar$ is Planck's constant, and B is the applied magnetic field. The two-electron spin qubit will oscillate between the S and T_0 states at a frequency $2\pi f = \Delta\omega = \Delta g\mu_B B/\hbar$, where Δg is the difference in electron g-factor between the two QDs. Z-rotations can be turned on by shifting the detuning closer to the charge anti-crossing where J is larger, driving oscillations around the equator of the Bloch sphere, Fig 1(c). The spin state is detected using Pauli blockade, combined with a remote charge sensor that detects whether the qubit state passed through the $(2,0)$ charge state or was blockaded in $(1,1)$ during the readout stage[38].

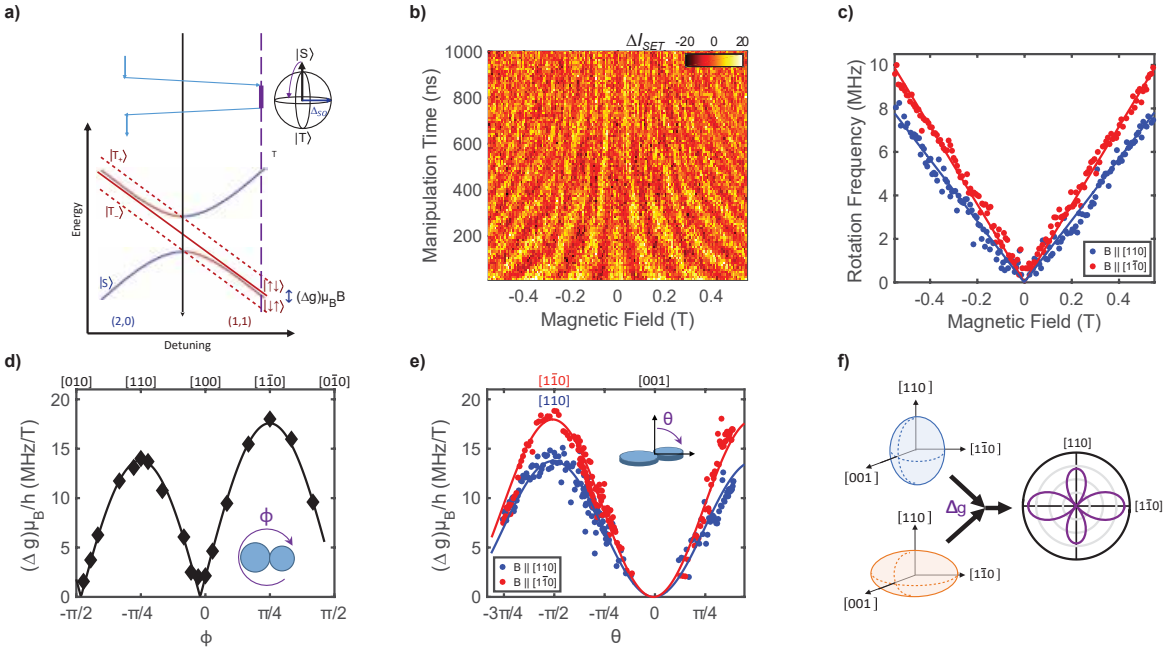

Fig. 2: **MOS interface spin-orbit interaction**. a) Energy diagram and gate pulse schematic for controlling spin-orbit rotations. We initialize the qubit into the S(2,0) ground state and transfer the system to the (1,1) charge sector with a rapid adiabatic pulse, such that it remains a singlet. The difference in Zeeman splitting between the QDs drives X-rotations between the $S(1,1)$ and $T_0(1,1)$ states. A rapid adiabatic return pulse projects the states onto the $S(2,0)$ and $T_0(1,1)$ basis for measurement. b) Change in charge sensor current as a function of X-rotation manipulation time as the magnetic field is varied along the $[1\bar{1}0]$ crystallographic direction. c) The extracted rotation frequency as a function of magnetic field strength along the [110] and $[1\bar{1}0]$ crystallographic directions. d,e) Magnetic field angular dependence of the SO-driven difference in g-factor between the dots for the in-plane, θ, and out-of-plane, ϕ, directions, respectively. Fits to the form $(\Delta g)\mu_B B/h = |\mathbf{B}||\Delta\alpha - \Delta\beta\sin(2\phi)|\sin^2(\theta)$ are also plotted for $\theta = \pi/2$ (black), $\phi = 3\pi/4$ (blue) and $\phi = \pi/4$ (red). f) A cartoon representation of the angular dependence of the two QDs (left). The difference between the QD g-factors give an in-plane dependence represented by the cloverleaf plot on the right.

Spin-orbit-driven spin rotations

The spin splitting of an electron in a QD is governed by an effective Zeeman Hamiltonian of the form $H_{\text{eff}} = \frac{\mu_B}{2}\mathbf{B}\cdot\mathbf{g}\cdot\boldsymbol{\sigma}$, where $\mathbf{B}$ is the magnetic field vector, $\boldsymbol{\sigma}$ is the vector of Pauli spin matrices $(\sigma_x, \sigma_y, \sigma_z)$ and $\mathbf{g}$ is the electron g-tensor. An electron confined to an interface will have Rashba and Dresselhaus SO couplings of the form $H_R \propto \gamma_R\left(P_y\sigma_x - P_x\sigma_y\right)$ and $H_D \propto \gamma_D\left(P_x\sigma_x - P_y\sigma_y\right)$, respectively, where γ_R and γ_D are the relative coupling strengths. The operators σ_x, σ_y are Pauli spin matrices, while P_x, P_y are components of the kinetic momentum $\mathbf{P} = -i\hbar\nabla + e\mathbf{A}(\mathbf{r})$ along the [100], [010] direction, with $e > 0$ the elementary unit of charge and $\mathbf{A}(\mathbf{r})$ the vector potential. Including the H_R and H_D SO Hamiltonians perturbatively leads to an effective g-tensor of the form

$$\mathbf{g} = \begin{pmatrix} g_\perp - \frac{2}{\mu_B}\alpha & \frac{2}{\mu_B}\beta & 0 \\ \frac{2}{\mu_B}\beta & g_\perp - \frac{2}{\mu_B}\alpha & 0 \\ 0 & 0 & g_\parallel \end{pmatrix}, \tag{1}$$

where $g_\perp$ ($g_\parallel$) is the g-tensor component for the directions perpendicular (parallel) to the [001] valley of bulk silicon. Corrections to the g-tensor due to Rashba and Dresselhaus spin-orbit coupling are characterized by α and β, respectively. The strength of the SO interaction is predicted to depend on applied electric field, lateral confinement, valley-orbit configuration, and the atomic-scale structure of the interface (see Supplementary Note 1 and Refs. [6, 27, 28, 30]). Consequently, the local interfacial and electrostatic environments particular to each QD produce differences in effective g-tensor, Fig. 2(f). This will act as a difference in effective in-plane magnetic field, modifying the electron spin splitting between dots and drive rotations at a frequency

$$f_{\mathrm{rot}}(\theta,\phi) = \Delta_{\mathrm{SO}}(\theta,\phi)/h = (\Delta g(\theta,\phi))\mu_{\mathrm{B}}B/h = \frac{2}{h}|\langle S|H|T_0\rangle| = |\mathbf{B}||\Delta\alpha - \Delta\beta\sin(2\phi)|\sin^2(\theta), \tag{2}$$

where ϕ is the field direction in-plane of the interface with respect to the [100] crystallographic direction, θ is the out-of-plane angle relative to [001], and $\Delta\alpha$ and $\Delta\beta$ quantify the difference in Rashba and Dresselhaus g-tensor perturbations between the two QDs, respectively. Our theoretical model for the SO coupling associated with the interface is discussed in greater detail in Supplementary Note 1 and is informed by the previous work of Refs [6, 24–28].

In Fig. 2(b), we show the singlet return signal as a function of time spent at the manipulation point in $(1,1)$ as the external magnetic field is varied along the $[1\bar{1}0]$ crystallographic direction. The observed oscillations demonstrate the ability to control coherent rotations. The rotation frequency displays a clear magnetic field dependence. In Fig. 2(c), we plot the SO-induced rotation frequency as a function of field for both the [110] and $[1\bar{1}0]$ directions. The linear dependence on field is consistent with a g-factor difference between the two QDs ($f = (\Delta g)\mu_{\mathrm{B}}B/h$), whereas the difference in the slopes indicates an angular dependence for Δg. We plot the full angular dependence of the SO interaction in Figs. 2(d) and 2(e). Figure 2(d) shows the measured difference in gyromagnetic ratio between the dots, $(\Delta g)\mu_{\mathrm{B}}/h$, as a function of the in-plane angle ϕ relative to the [100] crystallographic direction. Dependence on the out-of-plane angle, θ, is shown in Fig. 2(e). Here, ϕ is fixed along the [110] ($[1\bar{1}0]$) direction and the measured difference in gyromagnetic ratio between the dots is plotted in blue (red) as the field is tilted out of the interface plane ($\theta = 0$ is along the [001] direction). Qualitatively, the angular dependence is consistent with a SO effect, slightly different in each QD, composed of Rashba and Dresselhaus contributions. Enhanced interface SO effects in Si have been surmised previously for in-plane magnetic field dependences[27, 28, 39–41]. We plot fits to equation (2) along with the data in Figs. 2(d) and 2(e). We extract relative SO parameters $\Delta\alpha = 1.89$ MHz T^{-1} and $\Delta\beta = 15.7$ MHz T^{-1}. The maximum useful magnetic field is limited by state preparation and measurement (SPAM) errors as the S-T_- splitting becomes comparable to $k_{\mathrm{B}}T$. The maximum rotation frequency achieved for the present electrostatic confinement was near 20 MHz for fields above 1 T along the $[1\bar{1}0]$ direction.

The ability to realize meaningful quantum information processing in MOS depends on the timescale over which environmental noise near the interface interacts with the qubit, Fig. 3(c,d). Although sparse, the background ^{29}Si nuclear spins are sufficient in number to produce a slowly varying effective magnetic field, an Overhauser field. Nuclear spin flip-flops lead to a time-variation of the Overhauser field that is quasi-static on the timescale of a single measurement instance, but can shift the rotation frequency in the time interval between measurements. A consequence of this effect is that the decay in time of the coherent oscillations depends on the measurement integration time, as has been observed previously in ST qubits [12, 42]. The longer an average measurement is done, the broader the distribution of spin configurations (i.e. Overhauser fields) sampled. The ensemble-averaged singlet return signal as a function of time spent driving rotations in the $(1,1)$ region, with an external magnetic field oriented along the $[1\bar{1}0]$ crystallographic axis, is shown in Fig. 3(a). The decay in oscillation amplitude fits a Gaussian form consistent with quasi-static noise [42], and characteristic inhomogeneous dephasing time, $T_2^\star$, is extracted assuming a functional time dependence of $\exp[-(t/T_2^\star)^2]$ for the oscillation decay envelope.

In Fig 3(b) we examine the dependence of our results on measurement time and magnetic field. We find a long-averaging inhomogeneous dephasing time of $T_2^\star = 1.6 \pm 0.6$ µs, which is consistent within an order of magnitude with other DQD experimental results[12, 19] and theoretical estimates[43–45] (see Supplementary Note 3) of the ergodic limit of the dephasing due to hyperfine coupling of the QD electron wave function with residual ^{29}Si. By measuring at faster timescales, an increased $T_2^\star \sim 4$ µs is observed. The absence of a magnetic field dependence suggests that the SO coupling does not contribute appreciably to $T_2^\star$. Therefore, the $T_2^\star$ observed at the MOS interface is consistent with expectations of the ^{29}Si enriched bulk Si and there is no evidence of additional noise due to the MOS interface at this enrichment level.

Characterization of MOS charge noise

A second axis of coherent control for ST qubits is achieved through the tunable exchange coupling of the $(1,1)$ and $(2,0)$ charge states. This leads to hybridization between the $(2,0)$ and $(1,1)$ charge states and an exchange

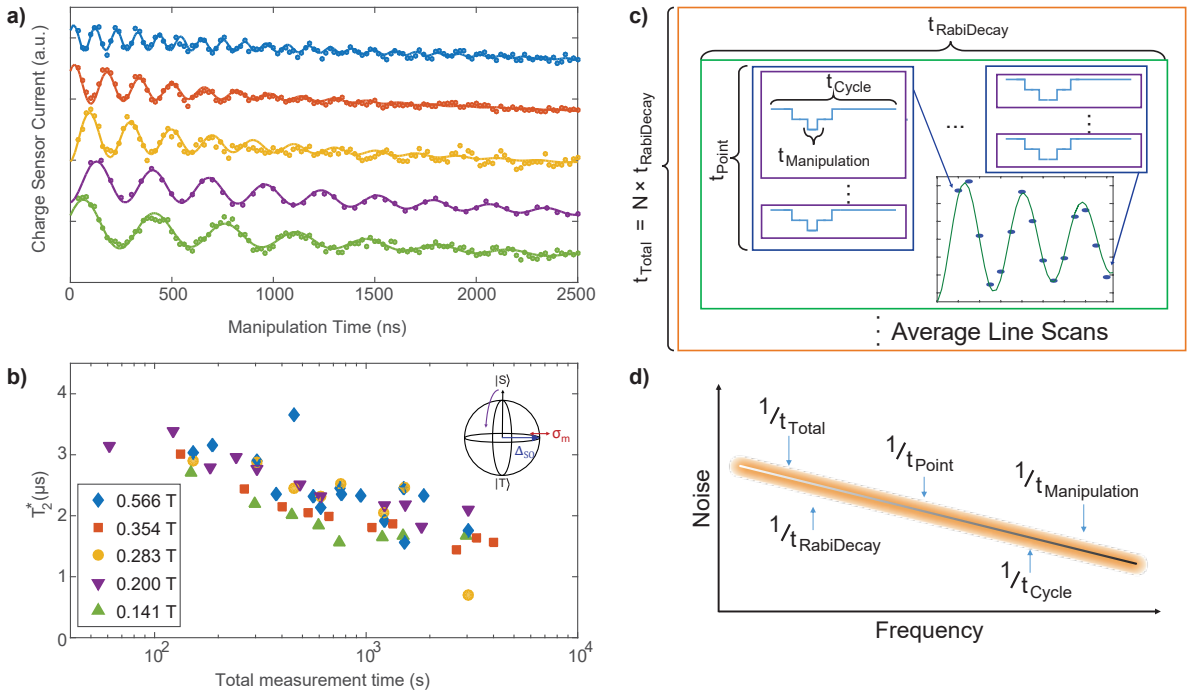

Fig. 3: **Measurement time dependence**. a) Long-time (50 min) averaged measurements of singlet return signal as a function of manipulation time for several magnetic field strengths aligned along the $[1\bar{1}0]$ crystallographic direction. The data for each field has been shifted for clarity. b) The extracted $T_2^\star$ as a function of total experimental measurement time. (inset) Magnetic noise creates fluctuations in the effective magnetic field at each QD, leading to variation in the X-rotation frequency throughout the measurement. c) Relevant time scales of the measurement. The shortest time scale susceptible to noise in the experiment is the time spent manipulating the qubit. In the limit of quasi-static noise, we expect the qubit to have a constant environment during this time. However, over the course of a total pulse cycle (which consists of qubit preparation and measurement and may be several ms in length), the environment may change. Furthermore, as the cycle is repeated and averaged by the lock-in for each data point, each data point is collected for a free induction decay curve. As successive curves are averaged together, the distribution of noise that is sampled grows larger. d) During the course of the measurement, the qubit is susceptible to noise in the frequency band between $1/\mathrm{t_{Total}}$ and $1/\mathrm{t_{Manipulation}}$.

splitting, $J(\epsilon)$, between the S and T_0 qubit states that depends on detuning, ϵ, Fig. 4(a). By varying the strength of this interaction, we can achieve controlled coherent rotations, as demonstrated in Fig. 4(b). Here, as described in Ref. [46], we initialize into a $S(2,0)$ ground state and then adiabatically separate the electrons into the $(1,1)$ charge configuration where $J(\epsilon)$ is nearly zero and the qubit is initialized in the ground state of the SO field ($|\uparrow\downarrow\rangle$ or $|\downarrow\uparrow\rangle$), a superposition of the $S(1,1)$ and $T_0(1,1)$ states. We apply a fast pulse to and from finite $J(\epsilon)$ at ϵ near 0 for some waiting time, which rotates the qubit state around the Bloch sphere about a rotation axis depending on both J and Δ_{SO}, the SO induced splitting of the $|\uparrow\downarrow\rangle$ and $|\downarrow\uparrow\rangle$ states (Fig. 4(a)). For this experiment, we apply a field of 0.2 T along the [100] direction, which provides a small (0.5 MHz) residual X-rotation frequency. At detuning near $\epsilon = 0$, we observe an increased rotation frequency, Fig 4(c). As the exchange pulse moves to deeper detuning, we observe a decrease in rotation frequency as well as visibility. This is expected as J decreases and the rotation axis tilts towards the direction of the SO field difference.

Figure 4(c) shows the observed rotation frequency as a function of detuning. The rotation frequency can be expressed as $\sqrt{J(\epsilon)^2 + \Delta_{\mathrm{SO}}^2}$, since the two components add in quadrature. Indeed, we see that at deep detuning the rotation frequency saturates near 0.5 MHz, due to the SO field at this magnetic field strength and orientation. Figure 4(d) shows the dephasing time, $T_2^\star$, associated with coherent rotations at each detuning. Here we have extracted $T_2^\star$ by fitting a Gaussian decay envelope ($\exp[-(t/T_2^\star)^2]$) to the rotations at each detuning point. Noise from charge fluctuations on the confinement gates causes deviations in the detuning point of the system, leading to dephasing of the qubit through changes in the rotation frequency. We measure shorter dephasing time near $\epsilon = 0$, which increases as we move to deeper detuning and eventually saturates at a few μs. We associate the saturation of $T_2^\star$ at deeper detuning with the dominant noise mechanism transitioning from charge to magnetic noise due to residual background ^{29}Si. Following the method outlined in Ref. [42], we fit the rotation frequency to a smooth function to find the

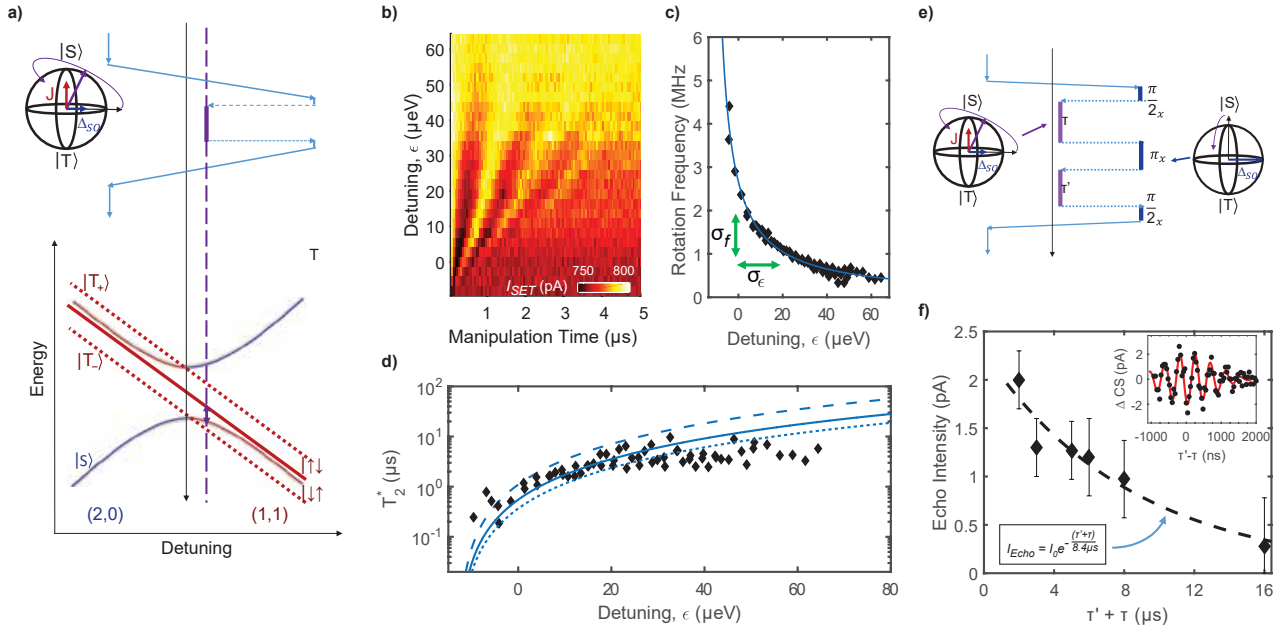

Fig. 4: Z **rotations and noise**. a) Energy Diagram and gate pulse schematic for controlling exchange rotations. We initialize the qubit into the S(2,0) ground state and ramp adiabatically, such that it transfers to the ground in the (1,1) charge sector. A fast pulse to and from a detuning, ϵ, where J is substantial drives coherent rotations around an axis depending on both J and Δ_{SO}. Returning to the (2,0) charge sector adiabatically projects the states onto the $S(2,0)$ and $T_0(1,1)$ basis for measurement. b) Measured charge sensor current as a function of the time spent rotating for various detuning points. Here, high current corresponds to a higher probability of measuring a singlet. c) The extracted rotation frequency vs. detuning. The blue line is a fit to the form $\sqrt{J(\epsilon)^2+\Delta_{\mathrm{SO}}^2}$, where $J(\epsilon)\propto\epsilon^{-1}$. d) Extracted $T_2^\star$ as a function of detuning. We also plot the long integration time values from Fig. 3(a). The blue lines are fits to the form $T_2^\star=\frac{1}{\sqrt{2\pi}\sigma_\epsilon}\cdot\left|\frac{\mathrm{d}f}{\mathrm{d}\epsilon}\right|^{-1}$, where the extracted charge noise, σ_ϵ, is 1.0 μeV (dashed), 2.0 μeV (solid) and 3.0 μeV (dotted). e) Gate pulse schematic for a Hahn-echo sequence. We initialize the qubit into the S(2,0) ground state and transfer the system to the (1,1) charge sector with a rapid adiabatic pulse such that it remains in a singlet state. Combinations of Δ_{SO}-rotations about the X-axis and J-rotations about a second axis provide access to entire Bloch sphere. This echo sequence counteracts low frequency noise, prolonging qubit coherence. f) Hahn-echo amplitude as a function of total time, $\tau'+\tau$, exposed to charge noise at detuning ϵ. The error bars represent 95% confidence interval. A fit to an exponential decay gives qubit coherence time of $T_{2e}^{\mathrm{echo}}=8.4$ μs. (inset) Measured echo signal for $\tau=1$ μs with B = 0.141 T along the [110] direction. The echo signal has an oscillation frequency corresponding to Δ_{SO} and a Gaussian envelope around $\tau=\tau'$ with a decay due to the inhomogeneous dephasing time of $T_{2e}^*=1$ μs.

derivative, $\mathrm{d}f(\epsilon)/\mathrm{d}\epsilon$. The ratio of $T_2^\star$ to $|\mathrm{d}f/\mathrm{d}\epsilon|^{-1}$ gives a root-mean-squared charge noise of $\sigma_\epsilon=2.0\pm0.6$ μeV. This agreement with the best reported charge noise values in GaAs/AlGaAs and Si/SiGe material systems of a few μeV [16, 18, 19, 42, 47] indicates that the poly-silicon MOS device structure is a competitive material system with respect to the magnitude of quasi-static charge noise. Furthermore, successive measurements over the course of several weeks can be performed with no retuning of the device gate voltages, indicating that the MOS material system is an extremely stable qubit platform.

Improved decoherence can be achieved through dynamical decoupling (DD), which suppresses contributions from quasi-static noise through multi-rotation sequences that leverage time reversal symmetry. A schematic for a Hahn-echo sequence to examine electrical noise is shown in Fig. 4(e). As seen in Fig. 4(f), a refocusing pulse can extend the qubit coherence with a $T_{2\mathrm{e}}^{\mathrm{echo}}$ of 8.4 μs for a detuning, ϵ, where charge noise leads to $T_{2\mathrm{e}}^*=1$ μs. This is comparable to what has been observed in GaAs/AlGaAs[42] and Si/SiGe[12]. Likewise, Hahn-echo techniques were able to improve decoherence from magnetic noise to a $T_{2\mathrm{m}}^{\mathrm{echo}}$ of 70 μs (see Supplementary Note 3). These results illustrate our ability to extend coherence times through dynamical decoupling and unequivocally demonstrate full all-electrical control of the MOS spin-orbit driven ST qubit.

DISCUSSION

In previous implementations of ST qubits, dynamic nuclear polarization (DNP)[48, 49], single nuclei [20, 21] and micro-magnets[19] have been used to create strong, stable difference in Zeeman splitting between two quantum dots to drive rotations. The SO driven X-rotations presented here reach 20 MHz and limited primarily by preparation and readout constraints (see Supplementary Note 3). Though this is larger than what has been reported for a ST qubit in Si/SiGe using a micro-magnet[19], it is smaller than the difference in Zeeman spin splitting of 50 to 1000 MHz between QDs reported in a number of other implementations mentioned above[20, 49, 50]. Increased drive frequency with SO coupling is likely possible through a number of avenues. Increasing the vertical electric field (see Supplementary Note 1 and Ref. [6]) and modifying the confinement potential (see Supplementary Note 1) will increase the strength of both the Rashba and Dresselhaus couplings.Additionally, the effect may be maximized by working with one of the QDs at higher occupation, since the two z-valleys at the hetero-interface are predicted to have opposite sign of the Dresselhaus strength (see SM and Refs. [6, 27, 28, 30]). Single QDs have displayed a 140 MHz difference in ESR frequencies between electron occupations of $N = 1$ and $N = 3$ and electric field tunability[6], so drive frequencies of over 100 MHz seem realistic.

On the other hand, our study of the angular dependence shows that by orienting the magnetic fields perpendicular to the interface, the difference in g-factor between the QDs is minimized. This is important for spin-qubit platforms where spin splitting variation is detrimental (e.g. spin-1/2 or exchange only qubits). This work also provides a theoretical foundation for the full angular dependence of an interface Dresselhaus and Rashba effect that avoids quantitative ambiguities due to gauge-dependence. Future work also remains to establish how the microscopic details of the MOS interface affects the magnitudes of the Rashba and Dresselhaus terms.

Most significantly from this work, the SO driven ST qubit is a sensitive probe of noise properties at the MOS interface. The $T_2^\star$ of order 1-2 µs observed in the magnetic noise dominated regime is consistent with the ergodic limit expected from ^{29}Si (i.e. order of magnitude agreement). Charge noise magnitudes of 2.0 ± 0.6 µeV at $T_e \sim 150$ mK are observed and are comparable to other semiconductor systems. Overall, the MOS interface shows no indication of increased negative effects relative to qubit operation despite the imperfect dielectric/crystal interface The opportunity to use MOS for highly sensitive spin coherent devices such as qubits has broad impact. Considering the possibilities for improvement and the reduced complexity in fabrication, the SO driven ST qubit offers a promising implementation for quantum information technology.

METHODS

DQD device and experimental set-up

The DQD studied in this work was realized in a fully foundry-compatible (i.e. subtractive processing), single-gate-layer, isotopically-enriched ^{28}Si metal-oxide-semiconductor (MOS) device structure. The material stack consists of 200 nm highly Arsenic-doped (5x10^{15} cm^{-2} at 50 keV) poly-silicon and 35 nm of silicon-oxide on top of a silicon substrate with an isotopically enriched epitaxial layer hosting 500 ppm residual ^{29}Si. Ohmic implants are formed using optical lithography and implantation of As at 3x10^{15} cm^{-2} at 100 keV. The confinement and depletion gates are defined by electron beam lithography followed by selective dry etching of the poly-silicon. Phosphorus donors were implanted (4x10^{11} cm^{-2} at 45 keV) through a self-aligned implant window near the QD locations for alternative experiments (see Refs. see [21] and [20]). This was followed by an activation annealing process at 900 C for 10 minutes in O_2 and 5 minutes in N_2 plus another 5 minutes in N_2 at 1000 C and a forming gas anneal at 400 C.

Biasing the poly-silicon gates confines a 2-dimensional electron gas into quantum dot potentials. One QD is used as a single electron transistor (SET) remote charge sensor for spin-to-charge conversion. The rest of the device is tuned such that a DQD is formed, where one QD, define by the gate geometry, is tunnel coupled to a second, non-lithographic, QD formed nearby. This second QD, though unintended, survives thermal cycling and is a built-in feature of this device. The number of electrons in each QD is inferred from changes in current through the SET. Measurements were performed in a ^{3}He/^{4}He dilution refrigerator with a base temperature of around 8 mK. The effective electron temperature in the device was 150 mK. Fast RF lines we connected to cryogenic RC bias tees on the sample board, which to allow for the application of fast gate pulses. An external magnetic field was applied using a 3-axis vector magnet. Additional information discussing the device and measurements is offered in the Supplementary Material and elsewhere[5].

Data availability

The authors declare that the data supporting the findings of this study are available within the paper and its Supplementary Information files. Additional data (e.g. source data for figures) are available from the corresponding author upon reasonable request.

[1] A. M. Tyryshkin, S. Tojo, J. J. L. Morton, H. Riemann, N. V. Abrosimov, P. Becker, H.-J. Pohl, T. Schenkel, M. L. W. Thewalt, K. M. Itoh, and S. A. Lyon, Nature Materials **11**, 143147 (2012).

[2] M. Veldhorst, J. C. C. Hwang, C. H. Yang, A. W. Leenstra, B. de Ronde, J. P. Dehollain, J. T. Muhonen, F. Hudson, K. M. Itoh, A. Morello, and A. S. Dzurak, Nature Nanotechnology **9**, 981 (2014).

[3] M. Veldhorst, C. H. Yang, J. C. C. Hwang, W. Huang, J. P. Dehollain, J. T. Muhonen, S. Simmons, A. Laucht, F. E. Hudson, K. M. Itoh, A. Morello, and A. S. Dzurak, Nature **526**, 410 (2015).

[4] J. K. Gamble, P. Harvey-Collard, N. T. Jacobson, A. D. Baczewski, E. Nielsen, L. Maurer, I. Montaño, M. Rudolph, M. S. Carroll, C. H. Yang, A. Rossi, A. S. Dzurak, and R. P. Muller, Applied Physics Letters **109**, 253101 (2016), http://aip.scitation.org/doi/pdf/10.1063/1.4972514.

[5] S. Rochette, M. Rudolph, A.-M. Roy, M. Curry, G. Ten Eyck, R. Manginell, J. Wendt, T. Pluym, S. M. Carr, D. Ward, M. P. Lilly, M. S. Carroll, and M. Pioro-Ladrière, arXiv.org (2017), arXiv:1707.03895.

[6] M. Veldhorst, R. Ruskov, C. H. Yang, J. C. C. Hwang, F. E. Hudson, M. E. Flatté, C. Tahan, K. M. Itoh, A. Morello, and A. S. Dzurak, Phys. Rev. B **92**, 201401 (2015).

[7] C. Jones, M. A. Fogarty, A. Morello, M. F. Gyure, A. S. Dzurak, and T. D. Ladd, (2016), arXiv:1608.06335.

[8] K. S. Ralls, W. J. Skocpol, L. D. Jackel, R. E. Howard, L. A. Fetter, R. W. Epworth, and D. M. Tennant, Phys. Rev. Lett. **52**, 228 (1984).

[9] D. Culcer and N. M. Zimmerman, Applied Physics Letters **102**, 232108 (2013), http://dx.doi.org/10.1063/1.4810911.

[10] A. Bermeister, D. Keith, and D. Culcer, Applied Physics Letters **105**, 192102 (2014), https://doi.org/10.1063/1.4901162.

[11] E. Kawakami, P. Scarlino, D. R. Ward, F. R. Braakman, D. E. Savage, M. G. Lagally, M. Friesen, S. N. Coppersmith, M. A. Eriksson, and L. M. K. Vandersypen, Nature Nanotechnology **9**, 666 (2014).

[12] K. Eng, T. D. Ladd, A. Smith, M. G. Borselli, A. A. Kiselev, B. H. Fong, K. S. Holabird, T. M. Hazard, B. Huang, P. W. Deelman, I. Milosavljevic, A. E. Schmitz, R. S. Ross, M. F. Gyure, and A. T. Hunter, Science Advances **1**, e1500214 (2015).

[13] D. M. Zajac, T. M. Hazard, X. Mi, K. Wang, and J. R. Petta, Applied Physics Letters **106**, 223507 (2015), https://doi.org/10.1063/1.4922249.

[14] X. Mi, C. G. Péterfalvi, G. Burkard, and J. R. Petta, Phys. Rev. Lett. **119**, 176803 (2017).

[15] J. S. Schoenfield, B. M. Freeman, and H. Jiang, Nat. Commun. **8**, 64 (2017).

[16] B. Thorgrimsson, D. Kim, Y.-C. Yang, L. W. Smith, C. B. Simmons, D. R. Ward, R. H. Foote, J. Corrigan, D. E. Savage, M. G. Lagally, M. Friesen, S. N. Coppersmith, and M. A. Eriksson, npj Quantum Information **3** (2017).

[17] M. G. Borselli, K. Eng, E. T. Croke, B. M. Maune, B. Huang, R. S. Ross, A. A. Kiselev, P. W. Deelman, I. Alvarado-Rodriguez, A. E. Schmitz, M. Sokolich, K. S. Holabird, T. M. Hazard, M. F. Gyure, and A. T. Hunter, Applied Physics Letters **99**, 063109 (2011), http://dx.doi.org/10.1063/1.3623479.

[18] Z. Shi, C. B. Simmons, D. R. Ward, J. R. Prance, R. T. Mohr, T. S. Koh, J. K. Gamble, X. Wu, D. E. Savage, M. G. Lagally, M. Friesen, S. N. Coppersmith, and M. A. Eriksson, Phys. Rev. B **88**, 075416 (2013).

[19] X. Wu, D. R. Ward, J. R. Prance, D. Kim, J. K. Gamble, R. T. Mohr, Z. Shi, D. E. Savage, M. G. Lagally, M. Friesen, S. N. Coppersmith, and M. A. Eriksson, Proceedings of the National Academy of Sciences **111**, 11938 (2014), http://www.pnas.org/content/111/33/11938.full.pdf.

[20] P. Harvey-Collard, N. T. Jacobson, M. lph, J. Dominguez, G. A. Ten Eyck, J. R. Wendt, T. Pluym, J. K. Gamble, M. P. Lilly, M. Pioro-Ladrière, and M. S. Carroll, Nat. Commun. **8**, 1029 (2017).

[21] M. Rudolph, P. Harvey-Collard, R. Jock, T. Jacobson, J. Wendt, T. Pluym, J. Domínguez, G. Ten-Eyck, R. Manginell, M. P. Lilly, and M. S. Carroll, arXiv.org (2017), arXiv:1705.05887.

[22] U. Rössler and J. Kainz, Solid State Communications **121**, 313 (2002).

[23] L. E. Golub and E. L. Ivchenko, Phys. Rev. B **69**, 115333 (2004).

[24] M. O. Nestoklon, L. E. Golub, and E. L. Ivchenko, Phys. Rev. B **73**, 235334 (2006).

[25] M. Prada, G. Klimeck, and R. Joynt, New Journal of Physics **13**, 013009 (2011).

[26] M. O. Nestoklon, E. L. Ivchenko, J.-M. Jancu, and P. Voisin, Phys. Rev. B **77**, 155328 (2008).

[27] R. Ferdous, E. Kawakami, P. Scarlino, M. P. Nowak, D. R. Ward, D. E. Savage, M. G. Lagally, S. N. Coppersmith, M. Friesen, M. A. Eriksson, L. M. K. Vandersypen, and R. Rahman, arXiv.org (2017), arXiv:1702.06210.

[28] R. Ferdous, K. W. Chan, M. Veldhorst, J. Hwang, C. H. Yang, G. Klimeck, A. Morello, A. S. Dzurak, and R. Rahman, arXiv.org (2017), arXiv:1703.03840.

[29] W. Huang, M. Veldhorst, N. M. Zimmerman, A. S. Dzurak, and D. Culcer, Phys. Rev. B **95**, 075403 (2017).

[30] R. Ruskov, M. Veldhorst, A. S. Dzurak, and C. Tahan, arXiv.org (2017), arXiv:1708.04555.

[31] P. S. Alekseev and M. O. Nestoklon, Phys. Rev. B **95**, 125303 (2017).

[32] T. Botzem, R. P. G. McNeil, J.-M. Mol, D. Schuh, D. Bougeard, and H. Bluhm, Nature Communications **7**, 11170 (2016).

[33] T. Fujita, T. A. Baart, C. Reichl, W. Wegscheider, and L. M. K. Vandersypen, npj Quantum Information **3** (2017).
[34] R. Maurand, X. Jehl, D. Kotekar-Patil, A. Corna, H. Bohuslavskyi, R. Laviville, L. Hutin, S. Barraud, M. Vinet, M. Sanquer, and S. De Franceschi, Nature Communications **7**, 13575 (2016).
[35] A. Manchon, H. C. Koo, J. Nitta, S. M. Frolov, and R. A. Duine, Nature Materials **14**, 871 (2015).
[36] A. Soumyanarayanan, N. Reyren, A. Fert, and C. Panagopoulos, Nature **539**, 509 (2015).
[37] D. A. Lidar, I. L. Chuang, and K. B. Whaley, Phys. Rev. Lett. **81**, 2594 (1998).
[38] P. Harvey-Collard, B. T. D'Anjou, M. Rudolph, N. Jacobson, J. Dominguez, G. A. Ten Eyck, J. R. Wendt, T. Pluym, W. A. Lilly, Michael Pand Coish, M. Pioro-Ladrière, and M. S. Carroll, arXiv.org (2017), arXiv:1703.02651.
[39] C. H. Yang, A. Rossi, R. Ruskov, N. S. Lai, F. A. Mohiyaddin, S. Lee, C. Tahan, G. Klimeck, A. Morello, and A. S. Dzurak, Nat Commun **4**, 2069 (2013).
[40] C. Tahan and R. Joynt, Phys. Rev. B **89**, 075302 (2014).
[41] J. C. C. Hwang, C. H. Yang, M. Veldhorst, N. Hendrickx, M. A. Fogarty, W. Huang, F. E. Hudson, A. Morello, and A. S. Dzurak, arXiv.org (2017), arXiv:1608.07748.
[42] O. E. Dial, M. D. Shulman, S. P. Harvey, H. Bluhm, V. Umansky, and A. Yacoby, Physical Review Letters **110**, 146804 (2013).
[43] L. V. C. Assali, H. M. Petrilli, R. B. Capaz, B. Koiller, X. Hu, and S. Das Sarma, Phys. Rev. B **83**, 165301 (2011).
[44] W. M. Witzel, R. Rahman, and M. S. Carroll, Phys. Rev. B **85**, 205312 (2012).
[45] W. M. Witzel, M. S. Carroll, L. Cywiński, and S. Das Sarma, Phys. Rev. B **86**, 035452 (2012).
[46] J. R. Petta, A. C. Johnson, J. M. Taylor, E. A. Laird, A. Yacoby, M. D. Lukin, C. M. Marcus, M. P. Hanson, and A. C. Gossard, Science **309**, 2180 (2005).
[47] K. Petersson, P. J.R., L. H, and G. A.C., Physical Review Letters **105**, 246804 (2010).
[48] S. Foletti, H. Bluhm, D. Mahalu, V. Umansky, and A. Yacoby, Nature Physics **5**, 903 (2009).
[49] J. M. Nichol, L. A. Orona, S. P. Harvey, S. Fallahi, G. C. Gardner, M. J. Manfra, and A. Yacoby, npj Quantum Information **3** (2017).
[50] K. Takeda, J. Kamioka, T. Otsuka, J. Yoneda, T. Nakajima, M. R. Delbecq, S. Amaha, G. Allison, T. Kodera, S. Oda, and S. Tarucha, Science Advances **2** (2016), 10.1126/sciadv.1600694.
[51] J. K. Gamble, N. T. Jacobson, E. Nielsen, A. D. Baczewski, J. E. Moussa, I. Montaño, and R. P. Muller, Physical Review B **91** (2015).
[52] M. Friesen, S. Chutia, C. Tahan, and S. N. Coppersmith, Phys. Rev. B **75**, 115318 (2007).
[53] D. Stepanenko, M. Rudner, B. I. Halperin, and D. Loss, Phys. Rev. B **85**, 075416 (2012).
[54] A. C. Johnson, J. R. Petta, C. M. Marcus, M. P. Hanson, and A. C. Gossard, Phys. Rev. B **72**, 165308 (2005).
[55] S. A. Studenikin, J. Thorgrimson, G. C. Aers, A. Kam, P. Zawadzki, Z. R. Wasilewski, A. Bogan, and A. S. Sachrajda, Applied Physics Letters **101**, 233101 (2012), https://doi.org/10.1063/1.4749281.
[56] J. D. Mason, S. A. Studenikin, A. Kam, Z. R. Wasilewski, A. S. Sachrajda, and J. B. Kycia, Phys. Rev. B **92**, 125434 (2015).
[57] T. Nakajima, M. R. Delbecq, T. Otsuka, P. Stano, S. Amaha, J. Yoneda, A. Noiri, K. Kawasaki, K. Takeda, G. Allison, A. Ludwig, A. D. Wieck, D. Loss, and S. Tarucha, Phys. Rev. Lett. **119**, 017701 (2017).
[58] M. A. Broome, T. F. Watson, D. Keith, S. K. Gorman, M. G. House, J. G. Keizer, S. J. Hile, W. Baker, and M. Y. Simmons, Phys. Rev. Lett. **119**, 046802 (2017).
[59] E. L. Hahn, Phys. Rev. **80**, 580 (1950).

ACKNOWLEDGEMENTS

We would like to thank Rusko Ruskov for discussions. This work was performed, in part, at the Center for Integrated Nanotechnologies, an Office of Science User Facility operated for the U.S. Department of Energy (DOE) Office of Science by Los Alamos National Laboratory (Contract DE-AC52-06NA25396) and Sandia National Laboratories (Contract DE-NA-0003525). Sandia National Laboratories is a multimission laboratory managed and operated by National Technology and Engineering Solutions of Sandia, LLC, a wholly owned subsidiary of Honeywell International, Inc., for the DOE's National Nuclear Security Administration under contract DE-NA0003525.

AUTHOR CONTRIBUTIONS

R.M.J, P.H.-C., and M.S.C. designed the experiments. R.M.J. performed the central measurements and analysis presented in this work. P.H.-C. performed supporting measurements on a similar device that establish repeatability of observations. N.T.J. developed the theoretical description of the results with the help of A.M.M., V.S., J.K.G., A.D.B., and W.M.W., providing critical insights. R.M.J., M.S.C., N.T.J., P.H.-C., A.M.M. and M.R. analyzed and discussed central results throughout the project. D.R.W., J.A., R.P.M., J.R.W., T.P., and M.S.C. designed the process flow, fabricated devices, and designed/characterized the ^{28}Si material growth for this work. J.R.W. provided critical nanolithography steps. M.S.C. supervised the combined effort, including coordinating fabrication and identifying

modeling needs for the experimental path. R.M.J. and M.S.C. wrote the manuscript with input from all co-authors.

ADDITIONAL INFORMATION

Supplementary Information accompanies this paper.
Competing interests: The authors declare no competing financial interests.

SUPPLEMENTARY INFORMATION

SUPPLEMENTARY NOTE 1. Spin-orbit Coupling at the MOS Interface

While spin-orbit (SO) coupling in bulk silicon is weaker than in some other materials commonly used for quantum dot devices, such as GaAs and InAs, an interface introduces SO coupling that may significantly influence qubit operation. Such effects have been documented recently elsewhere in the case of a single quantum dot in silicon [2, 6, 11, 27, 28, 30]. Here, we detail our model for the SO coupling associated with the interface. Our theoretical treatment is informed by the previous work of Refs [6, 24–26].

The Hamiltonian for a single electron in a silicon quantum dot in an arbitrary uniform magnetic field $\mathbf{B}$, without SO coupling included, is given by

$$\begin{aligned} H_0 &= H_{\text{dot}} + H_{\text{Zeeman}} \\ &= \frac{P_x^2}{2m_\perp} + \frac{P_y^2}{2m_\perp} + \frac{P_z^2}{2m_\parallel} + V(\mathbf{r}) + \frac{\mu_{\text{B}}}{2}\mathbf{B}\cdot\mathbf{g}_0\cdot\boldsymbol{\sigma}, \end{aligned} \tag{3}$$

where $\mathbf{P} = -i\hbar\nabla + e\mathbf{A}(\mathbf{r})$ is the kinetic momentum ($e > 0$), $m_\perp = 0.19m_0$ ($m_\parallel = 0.98m_0$) is the transverse (longitudinal) effective mass, and $\mathbf{g}_0 = \text{diag}(g_\perp, g_\perp, g_\parallel)$ is the bulk g-tensor for silicon. We take our coordinate system to be aligned along the Cartesian [100], [010], [001] axes, with [001] the interface normal. The potential $V(\mathbf{r})$ includes electrostatic confinement from voltages applied to gate electrodes and details of the interface potential. Atomic-scale features at the interface, the potential barrier height, and the vertical electric field dictate the valley splitting and valley content of the valley-orbital eigenstates [4]. Due to the strong vertical confinement, the low-lying valley-orbital eigenstates include contributions only from the $\pm z$ conduction band minima. As a consequence of the weak bulk SO coupling in silicon, $g_\perp$ and $g_\parallel$ are close to the vacuum g-factor of 2.0. In our double quantum dot device the bulk g-factor anisotropy, being common to both dots, does not manifest in significant measurable effects. The specific gauge choice for $\mathbf{A}$ has no influence on any physical observables, and we emphasize that any theoretical analysis must be gauge-invariant. When necessary for numerical calculations, we choose the convenient gauge $\mathbf{A}(\mathbf{r}) = \frac{1}{2}\mathbf{B}\times\mathbf{r}$.

Assuming that we have found the valley-orbital eigenstates of the spin-independent part of H_0, H_{dot}, we now treat the SO coupling as a perturbation. Following Refs [6, 24–26], we take the SO interaction for an electron confined against an interface at $z = z_i$ to consist of both Rashba and Dresselhaus terms, $H_R = \gamma_R\delta(z - z_i)(P_y\sigma_x - P_x\sigma_y)$ and $H_D = \gamma_D\delta(z - z_i)(P_x\sigma_x - P_y\sigma_y)$, respectively [23]. We emphasize the importance of the interface-localized δ-function in these terms. As we will see, this leads to the SO coupling appearing at first order in perturbation theory, rather than second order if the SO coupling had taken the bulk form without the interface-localizing δ-function. This latter property can be seen from the fact that, for bound valley-orbital eigenstates $|v_k\rangle$, the diagonal momentum matrix elements vanish, $\langle v_k|\mathbf{P}|v_k\rangle = 0$, without approximation. This can be confirmed by applying the commutation identities $P_x = \frac{im_\perp}{\hbar}[H_0, x]$, $P_y = \frac{im_\perp}{\hbar}[H_0, y]$, and $P_z = \frac{im_\parallel}{\hbar}[H_0, z]$. However, the interface-constrained diagonal matrix elements $\langle v_k|\delta(z - z_i)\mathbf{P}|v_k\rangle$ may be non-zero, in general, due to the cyclotron orbits established by an applied magnetic field. Note that, due to the crystal symmetry of silicon, a vertical shift of a pristine (001) interface by $z \to z + a_0/4$, where $a_0 = 0.543$ nm is the lattice constant, is equivalent to an in-plane rotation by an angle $\pi/2$. Consequently, while a Rashba term $P_y\sigma_x - P_x\sigma_y$ is invariant, a Dresselhaus term $P_x\sigma_x - P_y\sigma_y$ must change sign under such a transformation[26], since a $\pi/2$ rotation maps $P_y \to P_x$, $P_x \to -P_y$, $\sigma_y \to \sigma_x$, and $\sigma_x \to -\sigma_y$. Hence, we assign the Dresselhaus coupling factor a dependence $\gamma_D(z_i) = \gamma_D\cos(4\pi z_i/a_0)$ to capture the rapidly oscillatory behavior of the sign of the Dresselhaus coupling as a function of interface position.

To proceed with identifying the contributions of H_{SO}, we must evaluate the interface-constrained momentum matrix elements $\langle v_k|\delta(z - z_i)\mathbf{P}|v_j\rangle$ as a function of the applied magnetic field, $\mathbf{B}$. We note that the effective SO coupling strengths γ_R and γ_D should be expected to depend intimately on the atomistic details of the interface [24–26]. For the purposes of this analysis, we wrap such details into Rashba and Dresselhaus coupling strengths α_R and β_D, respectively, and treat them as fit parameters. Future work will address the question of capturing the short length-scale physics of interface SO effects within a multi-valley effective mass theory framework[51], in the spirit of previous analyses of valley splitting statistics in the presence of interface disorder[4].

The valley composition of the valley-orbital eigenstates $|v_k\rangle$ is dictated by the relative phase between the $+z$ and $-z$ valley components. Within a simplified envelope function picture (see e.g. Ref. [52]), the low-lying valley components are given by

$$|+z\rangle = e^{ik_0 z}u_{+z}(\mathbf{r})\psi(\mathbf{r}) \tag{4}$$

$$|-z\rangle = e^{-ik_0 z}u_{-z}(\mathbf{r})\psi(\mathbf{r}), \tag{5}$$

where $k_0 = 0.84\pi/a_0$ is the position of the conduction band minimum, $u_{\pm z}(\mathbf{r})$ are the lattice-commensurate Bloch

functions for silicon's $\pm z$ conduction band minima, and $\psi(\mathbf{r})$ is an envelope function. The lowest two valley-orbital eigenstates are, then

$$|v_0\rangle = \frac{1}{\sqrt{2}}(|+z\rangle + e^{i\phi_\mathrm{v}}|-z\rangle) \tag{6}$$

$$|v_1\rangle = \frac{1}{\sqrt{2}}(|+z\rangle - e^{i\phi_\mathrm{v}}|-z\rangle), \tag{7}$$

where ϕ_v is the valley phase factor. As mentioned previously, the value of ϕ_v and the valley splitting $\Delta_\mathrm{vs} = \langle v_1|H_\mathrm{dot}|v_1\rangle - \langle v_0|H_\mathrm{dot}|v_0\rangle$ is dictated by details of the interface and associated confinement potential.

In particular, we approximate

$$\langle v_0|\delta(z-z_i)P_j|v_0\rangle = \frac{c}{2}\left(1+\cos\left(\phi_\mathrm{v}-2k_0z_i\right)\right)\langle\psi|\delta(z-z_i)P_j|\psi\rangle, \tag{8}$$

where

$$\langle\psi|\delta(z-z_i)P_j|\psi\rangle = \iint \mathrm{d}x\mathrm{d}y\ \psi^*(x,y,z_i)P_j\psi(x,y,z_i), \tag{9}$$

with $\psi(\mathbf{r})$ the envelope function and c an unknown real parameter that depends on details of the Bloch function at the interface. Similarly, for the first excited valley state we'd obtain

$$\langle v_1|\delta(z-z_i)P_j|v_1\rangle = \frac{c}{2}\left(1-\cos\left(\phi_\mathrm{v}-2k_0z_i\right)\right)\langle\psi|\delta(z-z_i)P_j|\psi\rangle. \tag{10}$$

To investigate the momentum matrix element $\langle\psi|\delta(z-z_i)P_j|\psi\rangle$ with respect to the envelope function, we have implemented a (valley-free) finite-difference discretization of a Hamiltonian for a quantum dot that is harmonically confined laterally, with a uniform vertical electric field F_z and an interface with energy offset U_0,

$$\begin{aligned} H = &\frac{P_x^2}{2m_\perp} + \frac{P_y^2}{2m_\perp} + \frac{P_z^2}{2m_\parallel} \\ &+\frac{1}{2}m_\perp\omega_x^2x^2 + \frac{1}{2}m_\perp\omega_y^2y^2 + F_zz + U_0\Theta(z) \end{aligned} \tag{11}$$

The harmonic confinement energies $\hbar\omega_x$, $\hbar\omega_y$ are allowed to be distinct, describing an anisotropically-shaped quantum dot. From qualitative fits to a numerical analysis, we find the following functional form for the matrix elements with respect to the ground state envelope function:

$$\langle\psi|\delta(z-z_i)P_x|\psi\rangle \approx (a - b\hbar\omega_x)F_z^{2/3}B_y \tag{12}$$

$$\langle\psi|\delta(z-z_i)P_y|\psi\rangle \approx -(a - b\hbar\omega_y)F_z^{2/3}B_x, \tag{13}$$

where for dot confinement energies of $\mathcal{O}(\mathrm{meV})$ we find $(b \times 1\ \mathrm{meV})/a \approx 2\%$. The $F_z^{2/3}$ dependence is consistent with what is expected for a triangular vertical confinement potential [6]. Notice that these matrix elements depend weakly on the lateral confinement energies, with the dominant dependence on the vertical electric field and transverse magnetic field. This qualitative functional dependence on magnetic and vertical electric fields is consistent with the analysis of Ref [6]. In Supplementary Fig. 5, we plot a representative momentum density, indicating the cyclotron orbits induced by the applied magnetic field.

Combining the envelope function and valley components together, we obtain the following functional form for the interface-constrained momentum matrix elements:

$$\begin{aligned} \langle v_0|\delta(z-z_i)P_x|v_0\rangle &\propto \left(1+\cos\left(\phi_\mathrm{v}-2k_0z_i\right)\right) \\ &\quad\times(a - b\hbar\omega_x)F_z^{2/3}B_y \\ &= \lambda(\phi_\mathrm{v}, z_i, F_z, \hbar\omega_x)B_y \end{aligned} \tag{14}$$

$$\begin{aligned} \langle v_0|\delta(z-z_i)P_y|v_0\rangle &\propto -\left(1+\cos\left(\phi_\mathrm{v}-2k_0z_i\right)\right) \\ &\quad\times(a - b\hbar\omega_y)F_z^{2/3}B_x \\ &= -\lambda(\phi_\mathrm{v}, z_i, F_z, \hbar\omega_y)B_x, \end{aligned} \tag{15}$$

where $\lambda(\phi_\mathrm{v}, z_i, F_z, \hbar\omega)$ is a function that encodes the dependence on valley phase, interface location, vertical electric field, and lateral confinement.

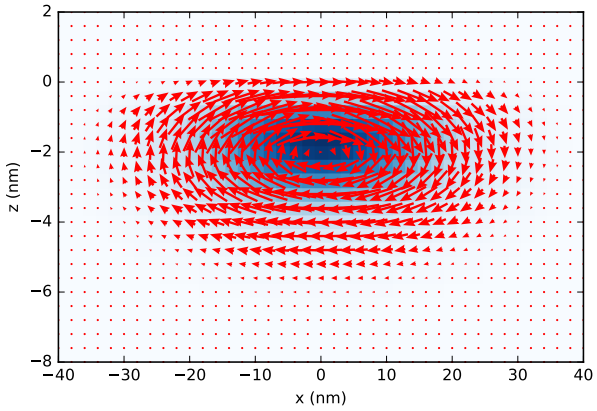

Fig. 5: **Quantum dot wave function**. Kinetic momentum density and cyclotron motion of the ground state of a quantum dot with an applied magnetic field $\mathbf{B} = B\hat{\mathbf{y}}$, for a slice at $y = 0$. In blue we show the probability density of the electron. The interface with offset $U_0 = 3$ eV is located at $z = 0$, vertical field is $F_z = 10$ MV m^{-1}, and lateral confinement energies are $\hbar\omega_x = 1$ meV, $\hbar\omega_y = 3$ meV. Notice that $\langle\psi|P_x|\psi\rangle = 0$, while $\langle\psi|\delta(z)P_x|\psi\rangle > 0$.

While the SO interaction will induce non-zero matrix elements between valley-orbital eigenstates such as $\langle v_0\uparrow|H_{\rm SO}|v_1\downarrow\rangle$, the influence of these matrix elements will be suppressed by the valley splitting $\Delta_{\rm vs}$ [6]. Since valley splitting in MOS systems is typically relatively large ($\mathcal{O}(100\ \mu$eV) in this experiment) and these inter-valley eigenstate matrix elements appear to second order in perturbation theory, we neglect them here.

Within the subspace spanned by the tensor product of the lowest valley-orbital eigenstate $|v_0\rangle$ and σ_z spin eigenstates $|\uparrow\rangle$, $|\downarrow\rangle$, $\{|v_0\uparrow\rangle, |v_0\downarrow\rangle$, we can express the SO Hamiltonian as

$$H_{\rm SO} = (-\gamma_R\lambda_y B_x + \gamma_D\lambda_x B_y)\sigma_x + (-\gamma_R\lambda_x B_y + \gamma_D\lambda_y)\sigma_y. \tag{16}$$

If we make the approximation that the dot is nearly symmetric, $\omega_x \approx \omega_y$, then this reduces to the form

$$\begin{aligned} H_{\rm SO} &= (-\alpha_R B_x + \beta_D B_y)\sigma_x + (-\alpha_R B_y + \beta_D B_x)\sigma_y \\ &= \frac{\mu_{\rm B}}{2}\mathbf{B}\cdot\mathbf{g}_{\rm SO}\cdot\boldsymbol{\sigma}, \end{aligned} \tag{17}$$

where

$$\mathbf{g}_{\rm SO} = \frac{2}{\mu_{\rm B}}\begin{pmatrix} -\alpha_R & \beta_D & 0 \\ \beta_D & -\alpha_R & 0 \\ 0 & 0 & 0 \end{pmatrix}. \tag{18}$$

Since we expect $a >> b\hbar\omega_{x,y}$, a non circular dot would include only small corrections to this form. Consequently, the interface SO interaction in a quantum dot can be represented as a modified g-tensor $\mathbf{g} = \mathbf{g}_0 + \mathbf{g}_{\rm SO}$, where

$$\mathbf{g} = \begin{pmatrix} g_\perp - 2\alpha_R/\mu_{\rm B} & 2\beta_D/\mu_{\rm B} & 0 \\ 2\beta_D/\mu_{\rm B} & g_\perp - 2\alpha_R/\mu_{\rm B} & 0 \\ 0 & 0 & g_\parallel \end{pmatrix}. \tag{19}$$

Note here that the total g-tensor $\mathbf{g}$ need not be symmetric, since any asymmetry in the quantum dot geometry may result in $g_{xy} \neq g_{yx}$, in general. However, in our fitting to the present experimental data we have observed satisfactory agreement when assuming a symmetric g-tensor. Future measurements with reduced statistical uncertainty or more anisotropic dot geometries may allow for this effect to be probed.

In the regime of deep detuning, for which the two electrons in the DQD are well delocalized into the $(1,1)$ charge configuration, we can treat the interface SO coupling as producing a distinct effective g-tensor in the left and right dots, $\mathbf{g}_L$ and $\mathbf{g}_R$. That is, the SO Hamiltonian transforms the Zeeman Hamiltonian for the two-electron problem into

$$H_{\rm Zeeman} = \frac{\mu_{\rm B}}{2}\mathbf{B}\cdot\mathbf{g}_L\cdot\boldsymbol{\sigma}_L + \frac{\mu_{\rm B}}{2}\mathbf{B}\cdot\mathbf{g}_R\cdot\boldsymbol{\sigma}_R, \tag{20}$$

where $\boldsymbol{\sigma}_L$ ($\boldsymbol{\sigma}_R$) is the vector of Pauli operators acting on an electron in the left (right) quantum dot.

We now show how this g-tensor difference appears in terms of the basis states $\{|S(1,1)\rangle, |T_+(1,1)\rangle, |T_0(1,1)\rangle, |T_-(1,1)\rangle\}$, where we follow the convention of Ref. [53]:

$$\begin{aligned}
|S(1,1)\rangle &= \frac{1}{\sqrt{2}}\left(c^\dagger_{L\uparrow}c^\dagger_{R\downarrow} - c^\dagger_{L\downarrow}c^\dagger_{R\uparrow}\right)|\emptyset\rangle \\
|T_+(1,1)\rangle &= c^\dagger_{L\uparrow}c^\dagger_{R\uparrow}|\emptyset\rangle \\
|T_0(1,1)\rangle &= \frac{1}{\sqrt{2}}\left(c^\dagger_{L\uparrow}c^\dagger_{R\downarrow} + c^\dagger_{L\downarrow}c^\dagger_{R\uparrow}\right)|\emptyset\rangle \\
|T_-(1,1)\rangle &= c^\dagger_{L\downarrow}c^\dagger_{R\downarrow}|\emptyset\rangle,
\end{aligned} \tag{21}$$

where $c^\dagger_{L\uparrow}$ ($c^\dagger_{R\uparrow}$) creates an electron in the left (right) quantum dot with spin up in the eigenbasis of σ_z (relative to the crystallographic axis [001]) and $|\emptyset\rangle$ is the zero-electron state. Given this set of basis states and defining

$$\begin{aligned}
\delta\mathbf{b} &= \frac{\mu_B}{2}\mathbf{B}\cdot(\mathbf{g}_L - \mathbf{g}_R)/2 \\
\bar{\mathbf{b}} &= \frac{\mu_B}{2}\mathbf{B}\cdot(\mathbf{g}_L + \mathbf{g}_R)/2,
\end{aligned} \tag{22}$$

we can now write down the Zeeman Hamiltonian incorporating SO coupling:

$$H_Z = \begin{pmatrix}
0 & -\sqrt{2}(\delta b_x + i\delta b_y) & 2\delta b_z & \sqrt{2}(\delta b_x - i\delta b_y) \\
\cdot & 2\bar{b}_z & \sqrt{2}(\bar{b}_x - i\bar{b}_y) & 0 \\
\cdot & \cdot & 0 & \sqrt{2}(\bar{b}_x - i\bar{b}_y) \\
\cdot & \cdot & \cdot & -2\bar{b}_z
\end{pmatrix},$$

where

$$\delta b_x = \frac{1}{2}(-B_x\Delta\alpha + B_y\Delta\beta) \tag{23}$$

$$\delta b_y = \frac{1}{2}(-B_y\Delta\alpha + B_x\Delta\beta) \tag{24}$$

$$\delta b_z = 0. \tag{25}$$

We now evaluate the unpolarized triplet spin eigenstate $|\tilde{T}_0(1,1)\rangle$ relative to the quantization axis dictated by the applied magnetic field, $\mathbf{B}$. Using the fact that the g-tensor is only weakly perturbed from its bulk value, $|\mathbf{g} - 2I| \ll 1$, and diagonalizing the 3x3 triplet block, we obtain

$$|\tilde{T}_0\rangle = \cos\theta|T_0\rangle + \frac{1}{\sqrt{2}}\sin\theta(e^{i\phi}|T_-\rangle - e^{-i\phi}|T_+\rangle), \tag{26}$$

where the applied magnetic field is taken to be

$$\mathbf{B} = |\mathbf{B}|(\sin\theta\cos\phi, \sin\theta\sin\phi, \cos\theta)) \tag{27}$$

with respect to the crystallographic axes [100], [010], and [001].

Finally, to evaluate the frequency of S/T_0 rotations generated by such a difference in g-tensors, we need to evaluate the matrix element $\langle S|H_{\rm SO}|\tilde{T}_0\rangle$, where $|S\rangle$ and $|\tilde{T}_0\rangle$ are the singlet and unpolarized triplet states defined with respect to the spin basis of the applied uniform magnetic field $\mathbf{B}$ defined above. We find that this rotation frequency is

$$f_{\rm rot} = \frac{2}{h}|\langle S|H_{\rm SO}|\tilde{T}_0\rangle| \tag{28}$$

$$= \frac{4}{h}|\sin\theta\big(\cos\phi\delta b_x + 2\sin\phi\delta b_y\big)| \tag{29}$$

$$= \frac{2}{h}|\mathbf{B}||\Delta\alpha - \Delta\beta\sin(2\phi)|\sin^2\theta. \tag{30}$$

From the above expression, it's clear that applying a magnetic field normal to the interface $\theta = 0$ will generate no

effective magnetic field gradient. For an in-plane field, depending on the relative sign of the Rashba and Dresselhaus differences $\Delta\alpha$ and $\Delta\beta$, there will be an azimuthal angle ϕ that maximizes the generated S/T_0 rotation frequency. If $\mathrm{sign}(\Delta\alpha) = \mathrm{sign}(\Delta\beta)$ ($\mathrm{sign}(\Delta\alpha) \neq \mathrm{sign}(\Delta\beta)$), the maximum rotation frequency will be obtained for $\phi = -\pi/4$ ($\phi = \pi/4$), i.e. magnetic field oriented along $[1\bar{1}0]$ ([110]). Conversely, for $|\Delta\beta| \gg |\Delta\alpha|$ the minimum rotation frequency would be obtained for $\phi \approx 0$ or $\pi/2$, i.e. nearly aligned along the [100] or [010] Cartesian axes. In our experiment, with $|\Delta\beta/\Delta\alpha| \approx 8.3$, the minimum frequency should be attained with a magnetic field about 3.5 degrees away from the [100] orientation.

SUPPLEMENTARY NOTE 2. Device Fabrication, Structure, Operation

Device Structure

The singlet-triplet (ST) qubit studied in this work was fabricated in a fully foundry-compatible process using a single-gate-layer, metal-oxide-semiconductor (MOS) poly-silicon gate stack with an epitaxially-enriched ^{28}Si epi-layer with 500ppm residual ^{29}Si. Hall bars from the same sample wafer with the same gate oxide were used to extract the critical density (n_c = 5.7x10^{11} cm^{-2}), the peak mobility (μ =4500 cm^2 V^{-1} s^{-1}), threshold voltage (V_{th} = 1.1 V), the RMS interface roughness (Δ = 2.4 Å), and roughness correlation length (λ = 26 Å). An SEM image of a device fabricated nominally identically to the one used in this work and a schematic of the gate stack are shown in Supplementary Fig. 6(a,b). The device is operated in an enhancement mode using voltage biasing of the highly doped n+ poly-silicon gates to confine electrons to quantum dot (QD) potentials under gates LCP and UCP. The gates ULG, URG, LLG and LRG overlap with n+ regions and ohmic contacts and are biased to accumulate a two-dimensional electron gas (2DEG) under each gate. The 2DEGs act as source and drain electron reservoirs for the quantum dots. The lower half of the device is tuned such that a double quantum dot (DQD) is formed. One QD is tunnel coupled to the reservoir under LRG and the other quantum dot can only be occupied by electron tunneling through the first QD. The upper half of the device is used as a single electron transistor (SET) remote charge sensor. The SET is biased with 70 μV (rms) AC bias at 0V DC and the current is measured with an AC lock-in technique at 979 Hz. The electron temperature, $T_e \sim 150$ mK, was measured by QD charge transition line width. More details about fabrication can be located in Ref [5].

Dot Occupation and Location

The number of electrons in each QD may be inferred from changes in current through the SET as depicted in Supplementary Fig. 6(c). The collection of yellow parallel lines is assigned to a QD connected to the electron reservoir under LRG, which we call QD_1. Counting from the left, we can identify the QD_1 N=1 $\rightarrow$ N=2 charging transition. A second object is observed anti-crossing with QD_1, which we label as the N=0 $\rightarrow$ N=1 charge transition for a second QD, QD_2. A second line is observed belonging to QD_2 in the scan, though disorder in the system makes identifying higher occupation lines difficult. However, the presence of Pauli spin blockade at the QD_1-QD_2, (2,0)-(1,1) anti-crossing identifies the system as a useful DQD for a ST qubit (see Supplementary Fig. 7). To determine the locations of QD_1 and QD_2 we can use their capacitances to the nearby poly-silicon gates. By scanning combinations of the poly-silicon gates (as seen in Supplementary Fig. 6(c) for LLP and LCP), we can obtain the relative capacitance of both QDs to each gate compared to the capacitance of LCP, which has the strongest capacitive coupling to both QDs. We have tabulated the relative capacitances in Table I. These values allow for triangulation of the dot locations,

Table I: Gate capacitance to QDs relative to LCP

c_i/c_{LCP}	LLP	LRP	LI	RI	LLG	LRG
QD_1	0.18	0.33	0.24	0.16	0.29	0.35
QD_2	0.27	0.22	0.13	0.14	0.29	0.10

which we have indicated in S6(b) with open circles. We differentiate QD_2 from an implanted donor through several observations: (1) no hyperfine component in the rotation frequency, (2) the lack of rotations at 0 T magnetic field, (3) the ramp rates required for adiabatic transfer through the spin gap are slower than what is expected for a donor, and (4) the presence of additional lines corresponding to the QD. We find that this layout systematically produces objects near the central QD with these capacitances when the gates opposite the electron reservoir 2DEG are at low

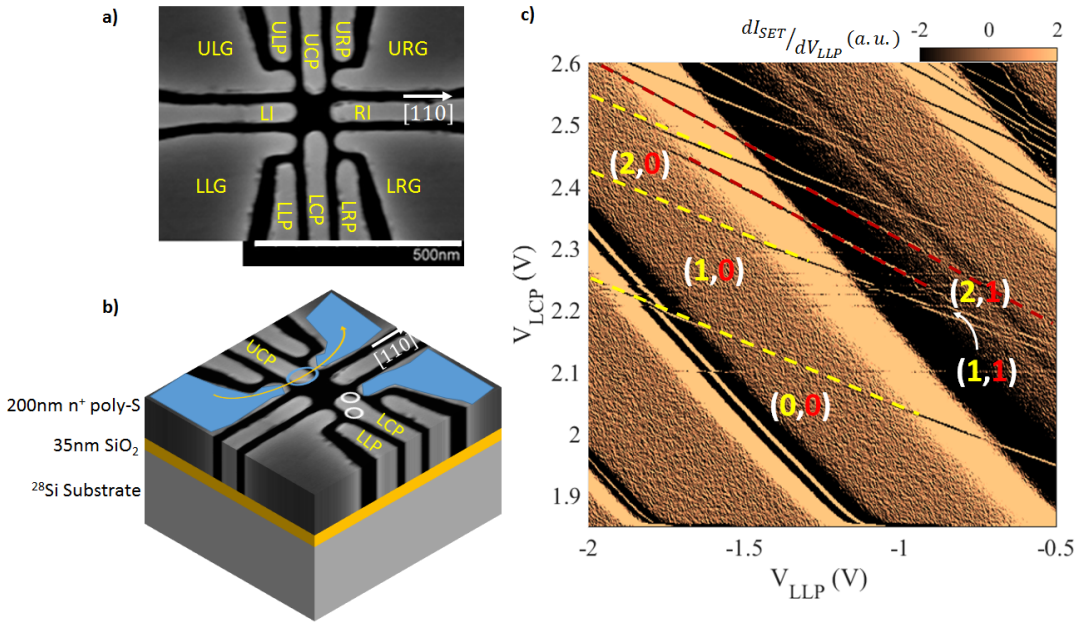

Fig. 6: **Device Structure**. a) A top-down SEM of the single-layer poly-silicon gate design. The gates are labeled in yellow and the [110] crystallographic direction is indicated in white. b) A cartoon schematic of the MOS gate-stack. The 2DEG reservoirs used in these experiments are illustrated in blue with the current through the top QD SET charge sensor depicted by the yellow arrow. The approximate locations of the two QDs are represented by the white circles. c) A charge stability diagram of the DQD. Here, the gradient of the current running through the SET charge sensor is plotted as the gates LLP and LCP are varied. The broad diagonal background features are due to Coulomb peaks of the SET charge sensor. The sharp features correspond to charge transitions of objects in the lower half of the device. QD_1 (the QD closer to the electron reservoir under gate LRG) is indicated by the successive yellow dashed lines, and QD_2 is indicated by the dashed red lines. The regions in gate space corresponding to different DQD charge occupations are labeled in parentheses with the occupation of QD_1 in yellow and QD_2 in red.

biases. For experiments investigating single QDs, these voltage potential minima may be emptied with more negative voltages on LLP or flooded by accumulating a larger 2DEG under LLG with more positive voltages.

Qubit Initialization, Operation and Readout

We operate this system near the (2,0) $\rightarrow$ (1,1) spin-blockaded (N_{QD_1}, N_{QD_2}) charge anti-crossing. An energy diagram for the two-electron system is shown in Supplementary Fig. 7(b). The ground state charge configuration is determined by the detuning between dots, ϵ, which is controlled by tuning the voltages on gates LLP and LCP. These gates are connected to cryogenic RC bias-Ts which allow the application of fast gate pulses. A schematic of the cyclical pulse sequence is shown in Supplementary Fig. 7(a), which is repeated as the current through the SET is monitored by the averaged AC lock-in measurements. The system is initialized in the (2,0) charge sector by first unloading (point U) the DQD into the (1,0) charge configuration and then applying an energy-selective pulse into the (2,0) charge state between the singlet and triplet energy levels such that a (2,0)S ground state is loaded (point L). The system is then plunged (point P) to a detuning ($\epsilon < 0$) close to the charge anti-crossing. The electrons are then separated (point C) and qubit manipulations are performed in the (1,1) charge region ($\epsilon > 0$). The system is then pulsed back to the (2,0) charge sector (point P) where, due to Pauli spin blockade, a singlet spin state is allowed to transfer to the (2,0) charge state, but a triplet spin state is energetically blocked and remains as a (1,1) charge state [54]. We then use an enhanced latching mechanism for a spin-to-charge conversion (pulsing to point M), where the triplet state is mapped to a (2,1) charge state. and the singlet is read out as (2,0). This technique relies on a slow tunnel rate from QD_2 to a charge reservoir. This causes singlet states to remain locked in a metastable (2,0) charge state when pulsing the system to point M, as a slow co-tunneling process is required to equilibrate. On the other hand, triplet states may quickly transfer to (2,1) by inelastically tunneling an electron onto QD_1 from the lead. There are several advantages for the use of this method. First, since an electron on the QD_2 needs to tunnel through the

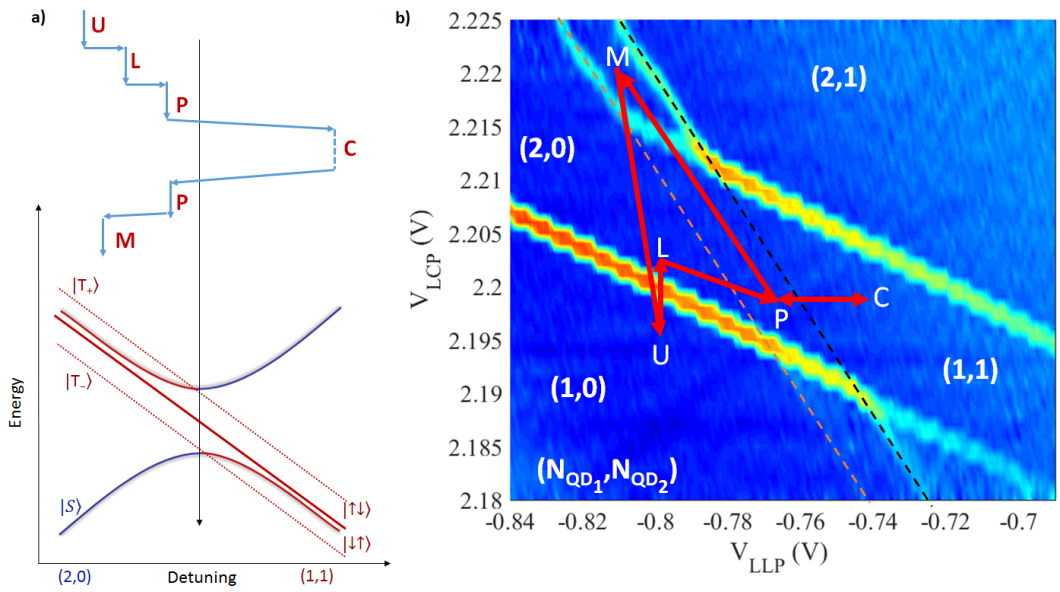

Fig. 7: **Qubit Operation**. a) Energy diagram and gate pulse schematic for qubit operations. b) A pulsed charge stability diagram for the (2,0) → (1,1) anticrossing, showing the gradient of the charge sensor current. The red arrows depict a general pulse sequence for controlling the qubit, where point C may consist of several detuning pulses for different qubit manipulation sequences. The black and orange dashed lines correspond to the location of the singlet and triplet state charge preserving lines, respectively. We do not observe a change in charge sensor current at the charge preserving lines due to the orientation of the DQD dipole.

QD_1 to access an electron reservoir, the metastable latching state can be long lived. This allows for the measurement step in our cyclical pulse sequence to be long, compared to other points in the sequence, and dominate the time average. Second, in this approach, the charge-sensed signal differentiates between a (2,1) and a (2,0) charge state. In other words, the difference in measured current between a singlet and triplet state is the capacitive effect of adding an electron to QD_2. Thus, it does not rely on the dipole orientation of the DQD, as in traditional Pauli-blockade measurement techniques. In our case, the DQD is oriented in such a way that differentiating a (2,0) and (1,1) charge state is exceptionally difficult (observe the lack of visible inter-dot transition line in Supplementary Fig. 7(b)) and this method is necessary. This technique is presented in greater detail in [38]. Additionally, the latching effect has been used to take advantage of the enhanced spin-to-charge signal and lifetimes in a variety of QD-QD[47, 55–57], donor-donor[58] and QD-donor[20, 38] coupled systems.

SUPPLEMENTARY NOTE 3. Analysis Note on Extracted Data

Qubit Rotation Frequency

Supplementary Figure 8(a) shows the singlet return signal as a function of time spent at the manipulation point in $(1, 1)$ as the strength of the external magnetic field is varied along the $[1\bar{1}0]$ crystallographic direction up to 1.2 T. We see that, at high magnetic field, the oscillations are difficult to observe, since the Coulomb blockade peak used for charge sensing drifts as a function of magnetic field. The qubit rotation frequency at each field was found by fitting each line scan to a Gaussian decay of the form

$$I_{SET} = A\sin(2\pi f t + \phi_0)\exp[-(t/T_2^\star)^2] + Bt + C \tag{31}$$

where all parameters are free. To help with the visualization, we subtract the background linear portion to our charge sensor signal ($Bt + C$, above), as shown in Supplementary Fig. 8(b).The background slope in charge sensor current is due to imperfectly separating the two electrons, such that, for some fraction of the experiments, an electron diabatically transitions through the ani-crossing, thus inelastically transferring between S(2,0) and S(1,1) on the time scale of a few μs. The rotation frequency, f, corresponding to the data in Supplementary Fig. 8(a) is plotted as

a function of magnetic field in Supplementary Fig. 8c, indicating a 20 MHz rotation frequency at the maximum field. As can be seen in Supplementary Fig. 7(c), there are outlier points, which occur when a fit to equation (31), produces an unphysical periodic component. Similar techniques were used to analyze the data in the main text. The

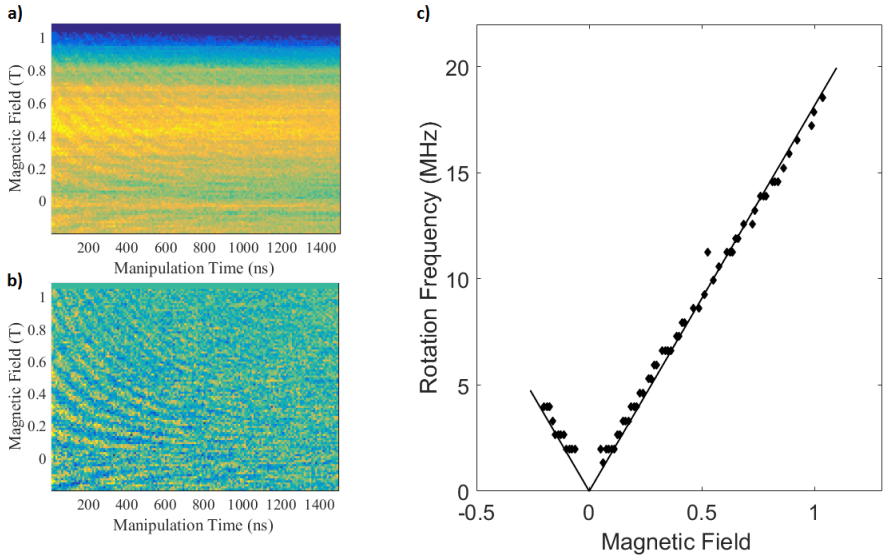

Fig. 8: **Qubit Rotation Frequency Scan**. a) Measured charge sensor current as a function of manipulation time as magnetic field is stepped. b) The measured data after subtracting the linear charge sensor background current. c) The extracted rotation frequency as a function of magnetic field. The solid line is a linear fit to magnetic field strength.

data presented in Figs. 2(c,e) of the main text were also obtained from magnetic field scan experiments and similar behavior was observed. A majority of the data fits well, and clear magnetic field strength and angular dependencies may be extracted. The data presented in Fig. 2(d), was taken with repeated scans at a given field strength and orientation. For Fig. 2(b), the linear portion of the background charge current sensor was subtracted, to clearly show the oscillations. This was useful, as slow timescale changes in the current through the charge sensor obscured the visualization.

Charge Noise Characterization

Here we describe the procedure to extract charge noise, following Ref [42]. Several results in ST qubits have shown that a dominant source of dephasing during exchange oscillations can be modeled as gate-referred, quasi-static voltage fluctuations on nearby gates[12, 42]. These voltage fluctuations affect the energy detuning between dots, materializing as fluctuations in the exchange energy, J. At a given detuning, the qubit will rotate at a frequency about the Bloch sphere

$$f(\epsilon) = \frac{1}{h}\sqrt{J(\epsilon)^2 + \Delta_{\mathrm{SO}}^2}. \tag{32}$$

Therefore, we expect noise in detuning $\delta\epsilon$ to create noise in the rotation frequency $\delta f \sim \delta\epsilon \cdot \mathrm{d}f/\mathrm{d}\epsilon$. For charge noise that is quasi-static, we expect a Gaussian decay of the oscillations of the form $\exp[-(t/T_2^\star)^2]$, where $T_2^\star$ is the inhomogeneous dephasing time which is related to the root-mean-squared charge noise by

$$\sigma_\epsilon = \frac{1}{\sqrt{2}\pi T_2^\star} \cdot |\mathrm{d}f/\mathrm{d}\epsilon|^{-1}. \tag{33}$$

$T_2^\star$ is found for each detuning point by fitting the oscillations to Gaussian decay as shown in Fig. 4(a) of the main text. A functional form of $f(\epsilon)$ is found by fitting the data in Fig. 4(c) to a smooth function. We approximate the exchange energy as $J(\epsilon) \approx t_c^2/4\epsilon$, where t_c is the full-gap, inter-dot tunnel coupling, and find a good fit to $f = \frac{1}{h}\sqrt{J(\epsilon)^2 + \Delta_{\mathrm{SO}}^2}$. We extract $t_c = 0.7$ μeV from the fit. From the ratio of $T_2^\star(\epsilon)$ to $|\mathrm{d}f/\mathrm{d}\epsilon|^{-1}$, for detunings less than 30 μeV, a charge

noise figure of $\sigma_e = 2.0 \pm 0.6$ μeV can be extracted. This value agrees with reported charge noise numbers of a few μeV[18, 19, 42, 47], indicating that proximity to the MOS interface does not degrade the qubit.

$T^*_{2\mathrm{m}}$ *Magnitude*

Several theoretical estimates of $T_2^\star$ in isotopically enriched silicon have been presented in the literature[43–45]. The estimate by Assali et. al. gives a $T_2^\star$ of 4.4 μs for the corresponding isotopic enrichment used in our experiments (500 ppm). Note: We have included a factor of 2 because the calculations in Ref. [43] do not account for $I = \frac{1}{2}$ of the ^{29}Si nuclei. Witzel et. al., on the other hand, predict a $T_2^\star$ of a few tens of μs, though they use a substantially larger QD radius. Following the central limit theorem, we expect $T_2^\star \sim \sqrt{N_S}$, where $\sqrt{N_S}$ is the number of spinful nuclei within the QD wavefunction, and that a decrease in QD size will lead to a decrease in the inhomogeneous dephasing time.

Furthermore, these reports consider single quantum dots. We are concerned with a DQD, in which each QD has a separate distribution of nuclear spins and the changes in the difference in hyperfine fields between QDs leads to the ST dephasing. Therefore, $T_2^\star$ is inversely proportional to the amount of fluctuations in the surrounding hyperfine field. If we say that each quantum dot has a normal distribution of hyperfine fields of the form

$$P = \frac{e^{-(x-\mu)^2/(\sigma^2_{\mathrm{QD}})}}{\sigma^2_{\mathrm{QD}}\sqrt{2\pi}}, \tag{34}$$

where σ_{QD} is the variance in hyperfine field and μ is the average hyperfine field, then the distribution of the difference in hyperfine field between the two dots is given by,

$$P_{\mathrm{QD}_1-\mathrm{QD}_2} = \int_{-\infty}^{\infty}\int_{-\infty}^{\infty} \frac{e^{-x^2/(\sigma^2_{\mathrm{QD}_1})}}{\sigma^2_{\mathrm{QD}_1}\sqrt{2\pi}} \frac{e^{-x^2/(\sigma^2_{\mathrm{QD}_2})}}{\sigma^2_{\mathrm{QD}_2}\sqrt{2\pi}} \delta((x-y)-u)dxdy = \frac{e^{-|u-(\mu_{\mathrm{QD}_1}-\mu_{\mathrm{QD}_2})^2/[(\sigma^2_{\mathrm{QD}_1})+\sigma^2_{\mathrm{QD}_2}]}}{\sqrt{2\pi(\sigma^2_{\mathrm{QD}_1})+\sigma^2_{\mathrm{QD}_2})}}. \tag{35}$$

This is a normal distribution with a variance of $\sqrt{\sigma^2_{\mathrm{QD}_1}+\sigma^2_{\mathrm{QD}_2}}$ and an average difference in Hyperfine field of $(\mu_{\mathrm{QD}_1}-\mu_{\mathrm{QD}_2})$. Thus, we expect

$$T^*_{2,\mathrm{DQD}} = T^*_{2,\mathrm{QD}}/\sqrt{2}, \tag{36}$$

assuming similar sized QDs. Taking into account the differences in QD size and the effect of two QDs, which both imply a reduction in $T_2^\star$, our measured value of 1.6 μs fits well with these order of magnitude estimates.

Measurement Time Dependence of $T^*_{2\mathrm{m}}$

Figure 3(b) of the main text displays a clear dependence of $T_2^\star$ on the total experimental measurement time. This effect has been reported previously[12, 42], and is due to the time dynamics of the random hyperfine field from the residual 500 ppm ^{29}Si in the isotopically purified silicon host. Fluctuations in the polarization of the nuclei lead to varying magnetic fields at each QD between each experiment cycle. This leads to a varying qubit rotation frequency in each experimental cycle, which, as they are averaged together, lead to a decay in oscillation amplitude. As the experiment is measured for longer times, a larger sample of random nuclei polarization configurations, and a correspondingly larger distribution of qubit rotation frequencies is sampled.

To obtain the plot in Figure 3(b), we repeat a measurement of charge sensor current versus manipulation time many times. An example of such a plot is shown in Supplementary Fig. 9(a) for a magnetic field of 0.2 T along the [110] direction. By averaging various numbers of line scans together, we can examine the effect of measurement time on $T_2^\star$. Here, the total measurement time is the time for one experimental line scan times the number of scans averaged, and $T_2^\star$ is extracted by fitting the envelope of the averaged data to a Gaussian decay ($\exp[-(t/T_2^\star)^2]$). Examples of the averaged data for averaging 5 and 50 line scans are shown in Supplementary Fig. 9(b).

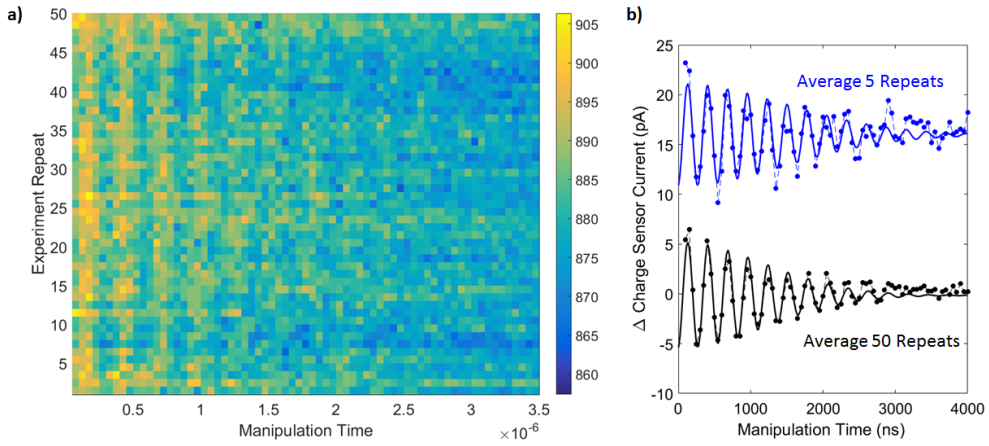

Fig. 9: **Measurement Time Dependence**. a) A repeated scan of charge sensor current vs. manipulation time for a magnetic field of 0.20 T along the $[1\bar{1}0]$ crystallographic direction. b) Singlet-triplet rotation decay plots. In black, all 50 scans are averaged and a fit to the data gives a T_2^* of 1.66 µs. When only 5 line scans are averaged (blue curve, shifted by 17 pA for clarity) a T_2^* of 2.09 µs is extracted.

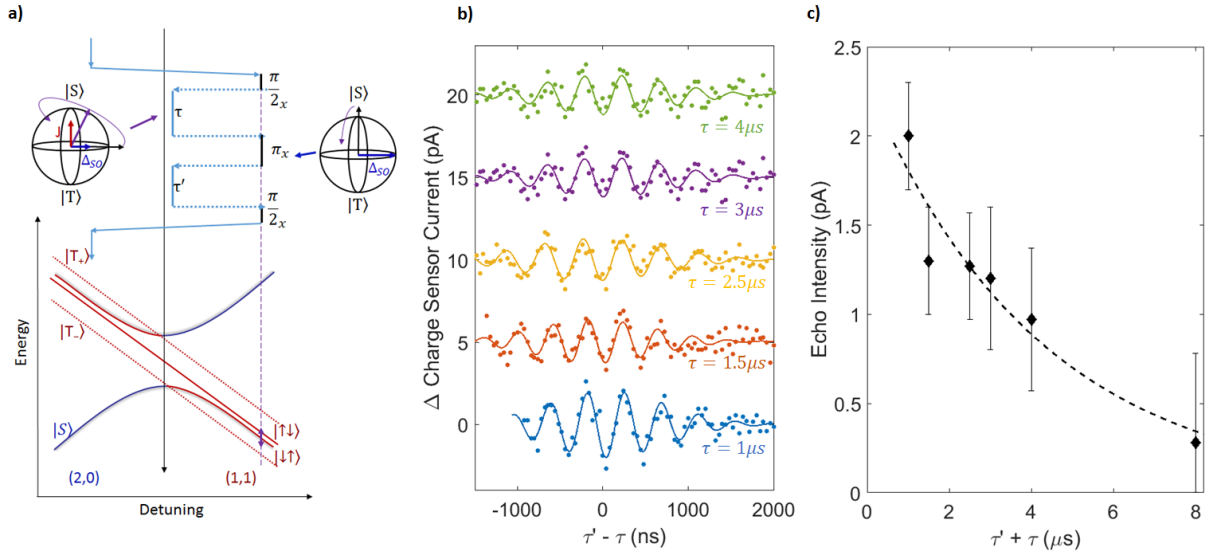

Fig. 10: **Charge Noise Hahn Echo**. a) The qubit is initialized in the S(2,0) ground state and a rapid adiabatic pulse transfers the system to the (1,1) charge sector such that it remains in a singlet state. The state is allowed to evolve for some time corresponding to $\pi/2$ pulse about the X-axis and rotates the spin state to the equator of the Bloch sphere. A pulse to a detuning, ϵ, where J is substantial for some time τ which causes the qubit to rotate about an axis depending on both J and Δ_{SO} at a frequency $f = \sqrt{(J(\epsilon))^2 + \Delta_{\mathrm{SO}}^2}$. Here the qubit is susceptible to charge noise and, as a consequence, begins to dephase. A π pulse about the X-axis flips the spin across the Bloch sphere where, upon returning to detuning ϵ, the dephased qubit states refocus for a time τ'. A final $\pi/2$-pulse around the X-axis returns the qubit to the ST basis and a rapid adiabatic return pulse projects the states onto the $S(2,0)$ and $T_0(1,1)$ basis for measurement. b) A Hahn-echo return for several τ values along with fits to a Gaussian envelope function. c) Hahn-echo amplitude as a functions of total time evolving under the effect of charge noise $(\tau' + \tau)$. The error bars represent 95% confidence interval. The dashed line is a fit to an exponential decay.

Hahn-Echo Measurements

The experiments presented in this work indicate that the dephasing of the qubit during rotations is predominantly due to low-frequency, quasi-static noise. Dynamical decoupling techniques may be used to prolong qubit coherence.

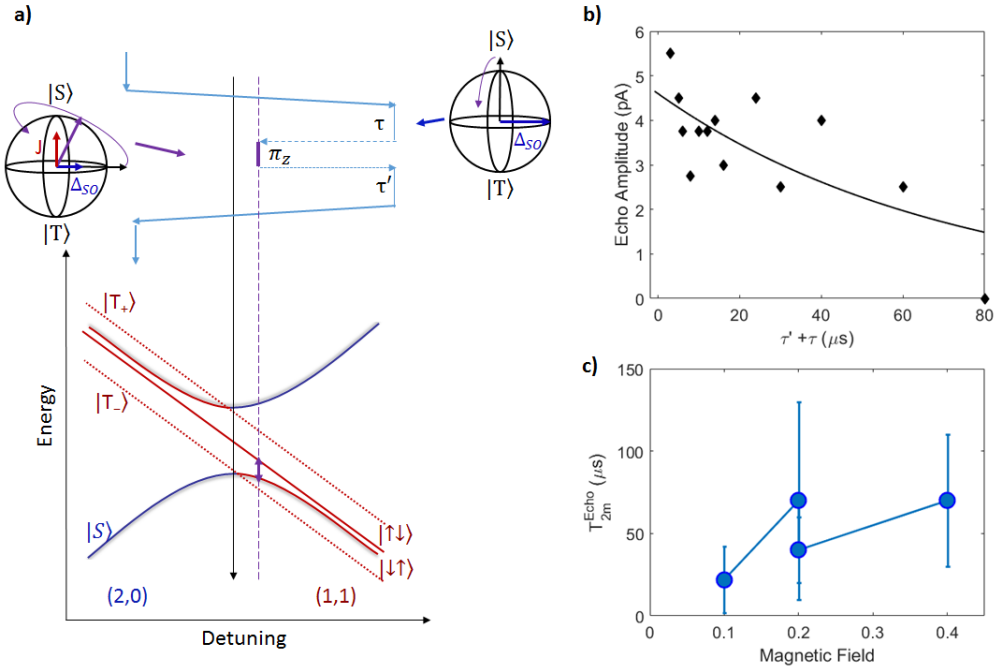

Fig. 11: **Magnetic Noise Hahn-Echo**. a) The qubit is initialized in the S(2,0) ground state and a rapid adiabatic pulse transfers the system to the (1,1) charge sector such that it remains in a singlet state where the state is allowed to evolve for some time, τ, about the X-axis under the influence of noise from magnetic fluctuations. A pulse to and from a detuning, ϵ, where J is substantial for a time corresponding to a π rotation about the axis depending on both J and $\Delta_{\rm SO}$ flips the spin across the Bloch sphere. The qubit states then evolve again for a time τ, refocusing the dephased qubit states. A rapid adiabatic return pulse projects the states onto the $S(2,0)$ and $T_0(1,1)$ basis for measurement. b) Hahn-echo amplitude as a functions of total time $(\tau+\tau)$ at a magnetic field of 0.2 T along the [100] crystallographic direction. The line is a fit to an exponential decay. c) The extracted $T_{2\rm m}^{echo}$ for several magnetic field values along the [100] direction. The error bars represent 95% confidence interval.

This method effectively filters the noise, such that qubit dephasing is most sensitive to noise around the experimental manipulation time. In this work we use a Hahn echo technique [59] to decouple from low frequency charge and magnetic noise. To perform a charge noise Hahn echo, a pulse sequence as detailed in Ref. [42] and depicted in Supplementary Fig. 10(a) is used. For the results presented in the main text, we operated the qubit at a magnetic field of 0.141 T along the [110] direction giving an X-rotation frequency of $\Delta_{\rm SO}/h = 2.03$ MHz. We investigate the effect of a Hahn echo pulse sequence on charge noise decoherence at a detuning where the qubit rotation frequency is 2.24 MHz, corresponding to $J/h = 0.99$ MHz ($f = \sqrt{J^2+\Delta_{\rm SO}^2}$). In Supplementary Fig. 10(b) the measured echo signal is plotted as a function of the difference in evolution times for the first and second J-pulse (τ' - τ) for several total evolution times $(\tau'+\tau)$. Here we have subtracted the background charge sensor current, leaving the echoed signal. The echo displays oscillations at 2.24 MHz and an overall Gaussian envelope corresponding to the inhomogeneous dephasing time. $T_2^\star$. By fitting the envelope to the form $A\exp[-((\tau'-\tau')/T_2^\star)^2]$, we can extract the echo amplitude, A, and the dephasing time, $T_2^\star$. We find an average dephasing time $T_2^\star = 1.02 \pm 0.06$ µs. In Supplementary Fig. 10(b) we plot the extracted echo amplitude as a function of the total evolution times $(\tau+\tau')$. The data reveals a clear decay in amplitude with a characteristic $1/e$ decoherence time of $T_{2\rm e}^{\rm echo} \sim 8.4$ µs. This is comparable to results observed in GaAs/AlGaAs[42] and Si/SiGe[12] ST qubits.

Similar pulse sequences may be used to decouple the qubit from low-frequency magnetic noise. As shown in Supplementary Fig. 11(a), we use a π pulse about the combined J and $\Delta_{\rm SO}$ axis to create a Hahn-echo. In Supplementary Fig. 11(b) the measured echo signal is plotted as a function of total evolution time under $\Delta_{\rm SO}$, $\tau'+\tau$, for a B = 0.2 T along the [100] crystallographic direction ($\Delta_{\rm SO}/h \sim 0.5$ MHz). An exponential fit reveals a $1/e$ decay time of $T_{2\rm m}^{\rm echo}$ $\sim$ 70 µs. The measured $T_{2\rm m}^{\rm echo}$ for several magnetic field strengths along the [100] is plotted in Supplementary Fig. 11(c). This value is shorter than other times reported for $T_{2\rm m}^{\rm echo}$ in silicon[12]. $T_2^{\rm echo}$ may be bounded by excitation to higher energy states or other T_1 processes, and further experiments are required to reveal the limiting mechanism. However, this result illustrates our ability to extend coherence times through dynamical decoupling and demonstrates

our full two-axis control over the qubit.

SUPPLEMENTARY REFERENCES.